MDPI

Article

Ozone Pollution in the North China Plain during the 2016 Air Chemistry Research in Asia (ARIAs) Campaign: Observations and a Modeling Study

Hao He [1,]*, Zhanqing Li [1,2] and Russell R. Dickerson [1,2]

[1] Department of Atmospheric and Oceanic Science, University of Maryland, College Park, MD 20742, USA; zhanqing@umd.edu (Z.L.); rrd@umd.edu (R.R.D.)
[2] Earth System Science Interdisciplinary Center, University of Maryland, College Park, MD 20740, USA
* Correspondence: haohe@umd.edu; Tel.: +1-301-314-1462

Abstract: To study air pollution in the North China Plain (NCP), the Air Chemistry Research in Asia (ARIAs) campaign conducted airborne measurements of air pollutants in spring 2016. High pollutant concentrations, with O_3 > 100 ppbv, CO > 500 ppbv, and NO_2 > 10 ppbv, were observed. CMAQ simulations with the 2010 EDGAR emissions capture the spatial and temporal variations in ozone and its major precursors such as NO_2 and VOCs, with significant underestimation. Differences between CMAQ simulations and satellite observations reflect changes in anthropogenic emissions, decreased NO_x emissions in megacities such as Beijing, but slight increases in other cities and rural areas. CMAQ also underestimates HCHO and CO, suggesting adjustments of the 2010 EDGAR emissions are necessary. $HCHO/NO_2$ column ratios derived from OMI measurements and CMAQ simulations show that VOC-sensitive chemistry dominates the ozone photochemical production in eastern China, suggesting the importance of tightening regulations on anthropogenic VOC emissions. After adjusting emissions based on satellite observations, better model performance was achieved. Because of the VOC-sensitive environment in ozone chemistry over the NCP, the underestimation of anthropogenic emissions could be important for CMAQ simulations, while future study and regulations should focus on VOC emissions with continuous controls on NO_x emissions in China.

Keywords: airborne measurements; ozone production sensitivity; OMI; CMAQ

1. Introduction

With rapid economic growth in the past three decades, the consumption of energy in China has increased dramatically [1–3]. Fossil fuels dominate total energy consumption, with coal still accounting for more than 50% of the carbon dioxide (CO_2) emissions in China [1]. This drastic increase in fossil fuel energy consumption has been accompanied by the deterioration of air quality [4,5], posing a threat to public health [6–9]. Particulate matter (PM) pollution, especially particulate matter with a diameter of less than 2.5 μm ($PM_{2.5}$) in the North China Plain (NCP), drew public concern and governmental actions [10–16]. PM pollution also has complex interactions with the planetary boundary layer (PBL) and its evolution, which can further degrade the air quality [17,18]. Recent studies showed that tropospheric ozone (O_3) pollution increased in China, exacerbating its complex air pollution problem [19–28].

Elevated ozone concentrations have adverse impacts on both human health [29–31] and the ecosystem [32–34]. Tropospheric ozone absorbs thermal radiation and acts as the third most important anthropogenic contribution to radiative forcing of climate [35–37]. In the lower troposphere, the photolysis of ozone is an important source of atmospheric hydroxyl (OH) radicals that control the lifetimes of atmospheric species such as CO and volatile organic compounds (VOCs) [38–40]. Tropospheric ozone has a relatively long lifetime of several days to weeks [41,42], leading to significant long-range transport of

ozone and its precursors [43–45]. Thus, investigation of ozone pollution in China is essential to support national and international policy decisions for air quality and the climate.

Tropospheric ozone is produced through complex photochemical reactions of precursors including nitrogen oxides (NO_x = NO + NO_2) and VOCs in the presence of sunlight [46–49]. In China, the sectors of power generation, industry, and transportation are the dominant sources of NO_x emissions [50–52]. Before 2010, NO_x emissions in China increased substantially [53,54]. Analysis of satellite data revealed that recently, NO_x emissions have started decreasing in highly developed regions such as the Pearl River Delta (PRD), but still increased in other regions [55–57]. Anthropogenic VOC emissions had a similar increasing trend in the past decades [58–61] and are projected to increase in the future [62]. Therefore, the recent increase in tropospheric ozone in China could likely be explained by the enhanced anthropogenic emissions of ozone precursors.

Due to the complex O_3-NO_x-VOCs chemistry, we need to understand the photochemical regime for local ozone production, i.e., whether it is NO_x-sensitive or VOC-sensitive [63,64]. Duncan et al. [65] used the ratio of tropospheric columns of formaldehyde (HCHO) and nitrogen dioxide (NO_2) observed by the National Aeronautics and Space Administration (NASA) Ozone Monitoring Instrument (OMI) onboard the Aura satellite to characterize ozone sensitivity. Studies show that a NO_x-sensitive regime dominates in the United States, except in megacities such as Los Angles and New York City, where the local ozone production is in VOC-sensitive or transition regimes [65–67]. However, studies reported that VOC-sensitive and transition regimes for ozone photochemical production exist ubiquitously in China due to the large amount of NO_x emissions, especially over the NCP [67–70]. As such, although the current regulations in China focus only on reduction of NO_x emissions [71–73], air quality can also benefit from VOC controls [74,75].

Aircraft measurements are essential to study the precursor emissions, photochemical production, and transport of ozone pollution at regional scale, while airborne campaigns are sparse in China [76–80]. To better understand the characteristics of ozone pollution, the Air Chemistry Research in Asia (ARIAs) aircraft campaign was conducted in Hebei Province in the NCP during May–June 2016, and was affiliated with the Aerosol Atmosphere Boundary-Layer Cloud (A^2BC) experiment [81–84]. Concentrations of major air pollutants in the lower atmosphere were measured during 11 research flights over the NCP, which were conducted in association with NASA's Korea U.S. Air Quality Study (KORUS-AQ) campaign in downwind South Korea. Measurements collected by the ARIAs research flights and the A^2BC surface observations can provide a comprehensive dataset to thoroughly study the tropospheric ozone pollution and emissions of its precursors in China.

In this study, we evaluated anthropogenic emissions and ozone pollution in the NCP using a combination of aircraft measurements, satellite observations, and modeling results. The U.S. Environmental Protection Agency (EPA) Community Multiscale Air Quality (CMAQ) model was used to simulate the atmospheric chemistry for the ARIAs campaign. We evaluated the emission data through comparison with aircraft measurements and satellite products, and adjusted emissions to improve the CMAQ performance. Lastly, we investigated the sensitivity of ozone production derived from CMAQ simulations and OMI observations and discussed the future ozone pollution in China.

2. Materials and Methods

2.1. Aircraft Campaign in the NCP

With more than 250 million tons of iron and steel produced in 2016 (data from http://data.stats.gov.cn, accessed in 10 September 2018), Hebei Province in the NCP is the most industrialized area in China. Due to its high emissions and proximity to megacities Beijing and Tianjin, the Beijing-Tianjin-Hebei area had severe air pollution in the past decade [85,86]. In May and June 2016, the ARIAs aircraft campaign was conducted over Hebei Province to investigate emissions, chemical evolution, and transport of air pollutants. The airborne campaign was coordinated with the A^2BC field campaign in Xingtai (XT, 37.18° N, 114.36° E, 182 m above sea level, ASL) and the NASA KORUS-AQ campaign to expand the

study to East Asia [81,87]. A Harbin Y12 research airplane (similar to the de Havilland Twin Otter) was employed to measure concentrations of air pollutants including O_3, carbon monoxide (CO), CO_2, and NO_2, and aerosol optical properties [81,88,89]. The research airplane was based in Luancheng airport (hereafter referred to as LC, 37.91° N, 114.59° E, 58 m ASL), south of Shijiazhuang, the capital city of Hebei province with 10 million population. Eleven research flights were conducted during the ARIAs campaign (Figure S1 in the Supplementary Materials). Vertical profiles of air pollutants from near-surface (~100 m above ground level, AGL) to the free troposphere (>3000 m) were conducted over LC, XT (the supersite of the A^2BC campaign), Julu (JL, 37.22° N, 115.02° E, 30 m ASL), and Quzhou (QZ, 36.76° N, 114.96° E, 40 m ASL).

The airborne measurements of ozone were conducted using a commercially available analyzer (Model 49C, Thermo Environmental Instruments, TEI, Franklin, MA, USA) [90]. NO_2 was measured using a modified commercially available cavity ring-down spectroscopy (CRDS) detector [91,92]. Nitrogen oxide (NO) and reactive nitrogen compound (NO_y) concentrations were analyzed using a commercially available NO analyzer (Model 42C, Thermo Environmental Instruments) with a hot molybdenum convertor working at 375 °C [93,94]. Ambient gas input was switched with and without the converter frequently to measure NO and NO_y simultaneously. However, due to high power demand of the instrument and converter, NO and NO_y were only measured during some research flights. Concentrations of CO and CO_2 were monitored with a 4-channel Picarro CRDS instrument (Model G2401-m, Picarro Inc., Santa Clara, CA, USA), calibrated with CO/CO_2 standards certified at the National Institute of Standards and Technology [95]. All the instruments were routinely serviced, calibrated and used for airborne measurements in the United States and China [79,90,95–99]. Detailed information about the instrumentation including the sampling frequency, precisions and accuracies is listed in Table S1 of the Supplementary Materials. Measurements of ambient air pollutants were logged at 1 Hz frequency, but the average times for different instruments were different, as shown in Table S1. All measurements were synchronized based on the Picarro measurements of CO_2 and CO with time, geolocation, and altitude from the Global Positioning System (GPS). The delay and lag time of each instrument was considered during the post-processing of observation data and averaged to a 1-minute record for further analysis and model evaluation.

In the ARIAs research flights, 28 whole air samples (WAS) were collected in vertical spirals at different altitudes from ~400 m to ~3500 m. The WAS were analyzed using gas chromatography (GC) with Flame Ionization Detection (FID) and Mass Spectroscopy (MS) by the College of Environment Sciences and Engineering at Peking University. Seventy-four species of alkanes, alkenes/alkynes, aromatics, and halocarbons were identified and quantified for a study on ozone photochemical chemistry (see details in [88,100]). Detection limits for the compounds ranged from 2 to 60 pptv. Hourly surface O_3, CO, and NO_2 concentrations for May and June 2016 were obtained from the public website of the China Ministry of Ecology and Environment (CMEE, available at https://quotsoft.net/air/ (accessed on 15 February 2020). The CMEE network had ~1450 monitoring sites in 2016 (Figure S2 in the Supplementary Materials). The units of CMEE measurements for O_3/NO_2 and CO are $\mu g/m^3$ and mg/m^3, respectively. We converted them to parts per billion by volume (ppbv) and parts per million by volume (ppmv) at standard temperature and pressure (STP) for model evaluation.

2.2. Satellite Products

To evaluate the emissions and atmospheric chemistry in the NCP and greater East Asia, we used satellite observations of CO, NO_2, and HCHO for May and June 2016. The Measurements of Pollution In the Troposphere (MOPITT) instrument onboard the NASA Terra satellite retrieved CO column contents with ~10:30 a.m. local overpass time [101]. We used the latest version 7 MOPITT Level 3 daily gridded average products ($1° \times 1°$ spatial resolution, available at https://eosweb.larc.nasa.gov/project/mopitt/mop03j_v007, accessed on 15 February 2020) for the ARIAs campaign period [102]. MOPITT thermal-

infrared and near-infrared (TIR + NIR) products show improved sensitivity to near-surface CO in China [103]. We used MOPITT near-surface CO (~900 hPa) products and related averaging kernels (AKs) to evaluate the CMAQ results [104].

OMI, onboard the NASA Aura satellite, is a UV/Vis solar backscatter spectrometer in a polar sun-synchronous orbit with a ~1:35 p.m. local overpass time. With high spatial resolution (13 km × 24 km for the center at nadir) and nearly daily coverage, OMI provided monitoring of trace gases and aerosol properties from 2005 [105]. The Version 3 OMI Level 2 NO_2 products (https://disc.gsfc.nasa.gov/datasets/OMNO2_V003/summary, accessed on 15 February 2020) [106] were used to evaluate the emissions and atmospheric chemistry in East Asia. Under clear sky, tropospheric NO_2 columns from OMI have precision of ~0.5×10^{16} molecules cm^{-2} and an accuracy of ±30% [107]. OMI HCHO Version 3 Smithsonian Astronomical Observatory (SAO) (https://disc.gsfc.nasa.gov/datasets/OMHCHO_V003/summary, accessed on 15 February 2020) Level 2 products were used in this study [108,109]. The precision of column HCHO is ~1.0×10^{16} molecules cm^{-2}, and SAO products have an accuracy of ±25–30% without clouds [110,111]. Data in OMI pixels affected by the row anomaly and contaminated by clouds were filtered out using quality flags for both NO_2 and HCHO columns.

2.3. Model Set-Up

We used CMAQ version 5.2 [112] to simulate atmospheric chemistry for the ARIAs campaign. The Weather Research and Forecasting (WRF) model Version 3.8.1 [113] was driven by the European Centre for Medium-Range Weather Forecasts (ECMWF) ERA-Interim products (ds627.0, https://rda.ucar.edu/datasets/ds627.0, accessed on 15 February 2020) [114] to generate meteorological fields. Two domains with spatial resolution of 36 km and 12 km (Figure 1) were used to cover East Asia, with 35 layers from the surface to 50 hPa and ~20 layers in the lowest 2 km. Major physical options in WRF include the Rapid Radiative Transfer Model (RRTM) radiation scheme [115], the Pleim-Xiu surface layer and land surface model [116,117], the Asymmetric Convective Model (ACM2) boundary layer scheme [118], the Kain–Fritsch cumulus scheme [119], and the WRF Single-Moment 6 (WSM-6) microphysics [120]. The National Centers for Environmental Prediction (NCEP) ADP Global Surface and Upper Air Observational Weather Data (ds461.0 and ds351.0, https://rda.ucar.edu, accessed on 15 February 2020) were used to perform observational and analysis nudging on all domains following the method developed for NASA aircraft campaigns [97,121]. WRF outputs were processed by the EPA Meteorology-Chemistry Interface Processor Version 4.3 (MCIP v4.3, released in November 2015) for emission processing and CMAQ simulations.
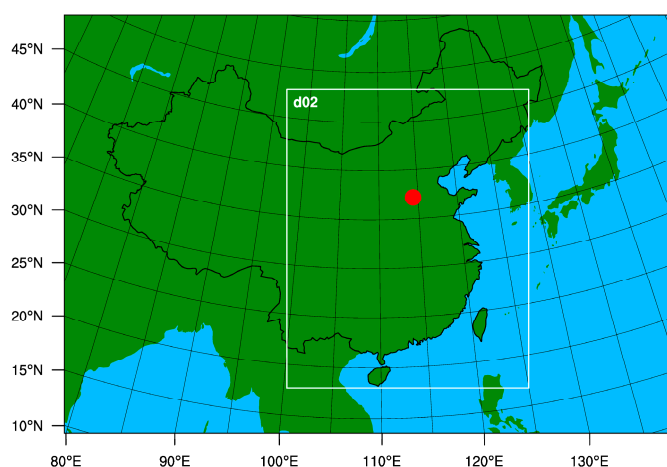

Figure 1. CMAQ domains for the ARIAs campaign (the proximate aircraft campaign area is demonstrated by a red dot). The coarse domain (d01, 36 km resolution) covers East Asia, and the nested domain (d02, 12 km resolution) focuses on eastern China.

Anthropogenic emissions data were from the Emissions Database for Global Atmospheric Research Version 4.2 (EDGAR v4.2, 0.1° × 0.1° resolution) for year 2010, which are widely used for chemical transport modeling [122]. We used the EPA Sparse Matrix Operator Kernel Emissions (SMOKE) modeling system Version 4.5 [123] to project EDGAR emissions to the modeling domain. Emissions of air pollutants were speciated into Carbon Bond 05 chemical mechanism [124] and updated AERO6 aerosol module [125]. The EDGAR v4.2 inventory has emissions for energy, industry, residential, and transport sectors. Without stack height information for power plants in the energy sector, we followed the approach developed in He et al. [99] to locate these anthropogenic emissions at ~200 m above the surface as an approximation for averaged stack height and plume rise. We used the United States Geological Survey (USGC) 24 category land use dataset combined with the Biogenic Emission Inventory System (BEIS) emission factors table to generate the input files for the CMAQ inline biogenic emissions modeling. Biogenic emissions were estimated using the BEIS module inline in CMAQ [112].

CMAQ v5.2 uses the updated Carbon Bond 6 (CB6r3) chemical mechanism [126] including improved chemistry mechanism for organic nitrates and peroxyacyl nitrates (PAN) chemistry and leads to better performance in simulating Secondary Organic Aerosols (SOA) and tropospheric ozone in the United States [127]. CMAQ was run with a coarse domain and a nested domain (Figure 1). Chemical initial and boundary conditions for the coarse domain were obtained from the default concentration profiles built in CMAQ [112]. Results from the CMAQ coarse domain were used to generate boundary conditions for the nested domain. The WRF-CMAQ system was run from mid-April to June, with the first 2 weeks as spin-up. Hourly concentrations of air pollutants were saved for further analysis and model evaluation.

3. Results

3.1. Air Pollution in the NCP and CMAQ Performance

Figure 2 summarizes all aircraft measurements of O_3, NO_2, CO, and CO_2 over the NCP from 11 research flights. Generally, we observed high concentrations of air pollutants, with maximum values as >100 ppbv of O_3, >20 ppbv of NO_2, >500 ppbv of CO, and >450 ppmv of CO_2, in the aircraft campaign area (defined as 36.5–38.5° N, 114.0–115.5° E hereafter). We conducted vertical spirals over XT (the A^2BC supersite), LC (the airport in south of Shijiazhuang), and two rural areas (JL and QZ) during the ARIAs research flights. Figure 3a summarizes vertical distributions and the mean profiles of air pollutants over XT, with mean O_3 concentrations of 80 ppbv in the lower atmosphere. We observed isolated plumes with >10 ppbv of NO_2, >1000 ppbv of CO, and >440 ppmv of CO_2 over XT, usually with a secondary maximum between 800 and 1200 m (a sample plume is presented in Figure S3 of the Supplementary Materials). These plumes aloft can play an important role in long-range transport of air pollutants to downwind regions. Profiles over LC (Figure 3b) show higher O_3 concentrations (>100 ppbv) and relatively moderate NO_2 (~3 ppbv) and CO (~250 ppbv). The rural areas, JL and QZ, have relatively clean environments with <80 ppbv of O_3, <2 ppbv of NO_2, and <300 ppbv of CO (Figure 3c,d). Even the concentrations of air pollutants over the rural region in the NCP are comparable to or higher than values in urban areas in North America and Europe. These results suggest both south–north and east–west gradients of air pollution in the campaign region, i.e., higher concentrations of air pollutants in the west XT-LC corridor near the mountain as compared with east side of JL-QZ, and higher concentrations in the north LC as compared with the south XT. The ARIAs research flights had good coverage of regions with both high and moderate concentrations of air pollutants and can fairly represent the regional nature of air pollution over the NCP.
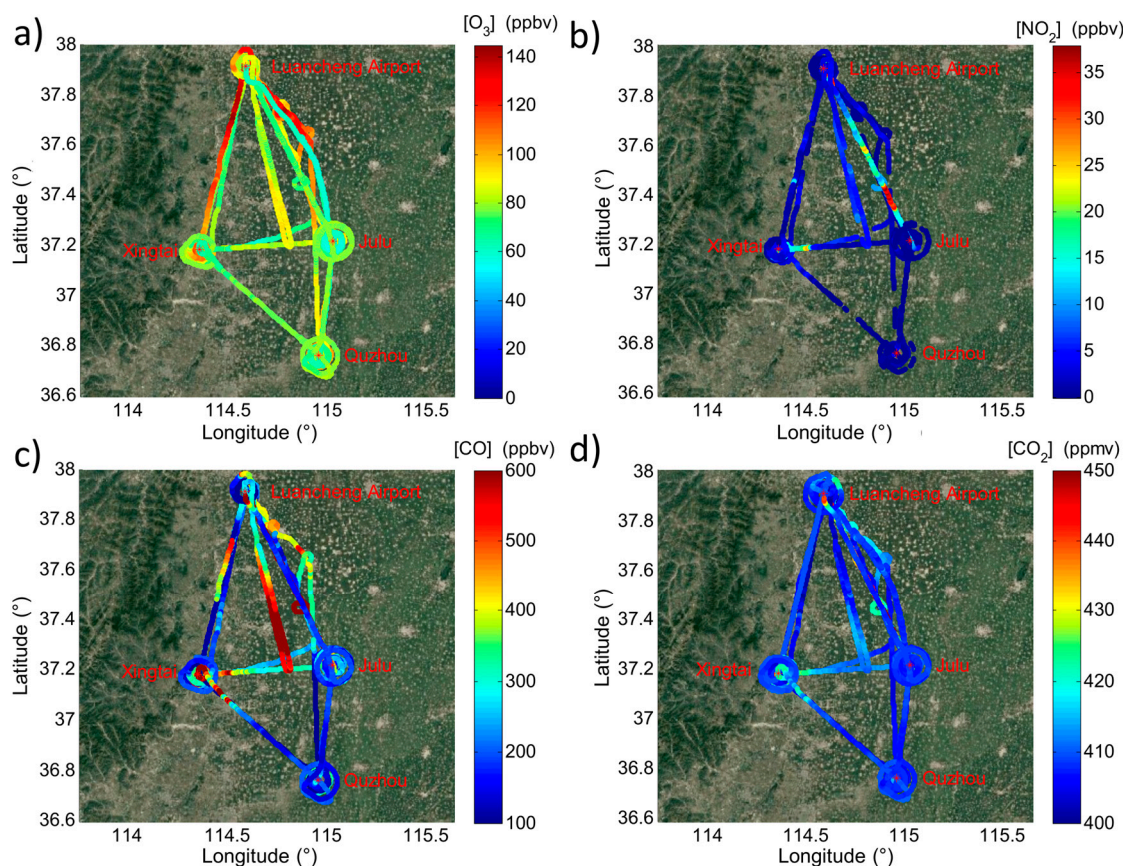
Figure 2. Summary of air pollutant concentrations over the NCP observed by Y12 aircraft. (**a**) O_3, (**b**) NO_2, (**c**) CO, and (**d**) CO_2.

To evaluate the model performance in eastern China, we compared the mean concentrations of daily 8-hour maximum (MDA8) ozone in May and June 2016 from CMEE observations and CMAQ simulations driven by the EDGAR inventory (named the CMAQ_baseline run hereafter). The CMAQ_baseline run slightly underestimates concentrations of surface ozone in eastern China but cannot reproduce high surface ozone in some cities in the NCP (Figure 4a), and the overall underestimate is moderate with a linear regression slope of 0.86 (Figure 4b). For CO and NO_2, two important ozone precursors, significant underestimations exist ubiquitously in eastern China (Figure S4 in the Supplementary Materials). These results suggest that the underestimation of ozone precursors in CMAQ could lead to poor model performance in simulating tropospheric ozone.

Similar analyses were conducted to investigate air pollutant concentrations in the lower troposphere over the NCP observed by the aircraft. A research flight on 11 June 2016 (Figure S5 in the Supplementary Materials) shows that CMAQ well captures the vertical gradient of air pollutants, while substantially underestimating concentrations of all trace gases except NO_y. Since CMAQ generated hourly outputs, to alleviate the uncertainty of comparing 1-minute aircraft data and hourly model simulations, we used 10-minute averaged aircraft measurements that were matched to the closest hourly model output following the approach described in Goldberg et al. [128]. Figure 5 shows similar underestimation (50% to 75% for all air pollutants) as compared with surface measurements (Figure 4 and Figure S4 in the Supplementary Materials). CMAQ overestimates NO_y but substantially underestimates NO and NO_2, which suggests that a significant amount of reactive nitrogen compounds could exist in the form of organic nitrates or nitrate aerosols in the model. Figure 6 compares total VOC concentrations from WAS samples and CMAQ simulations, indicating that VOC levels are also significantly underestimated by 80%. The model evaluation with surface and aircraft measurements suggests that ozone pollution in

the NCP has been significantly underestimated in the CMAQ_baseline run, which could be due to the uncertainty introduced by using the 2010 EDGAR emissions to simulate the 2016 ARIAs campaign period. Thus, we need to evaluate the emissions inventory data to improve the CMAQ performance and investigate the sensitivity of ozone production.
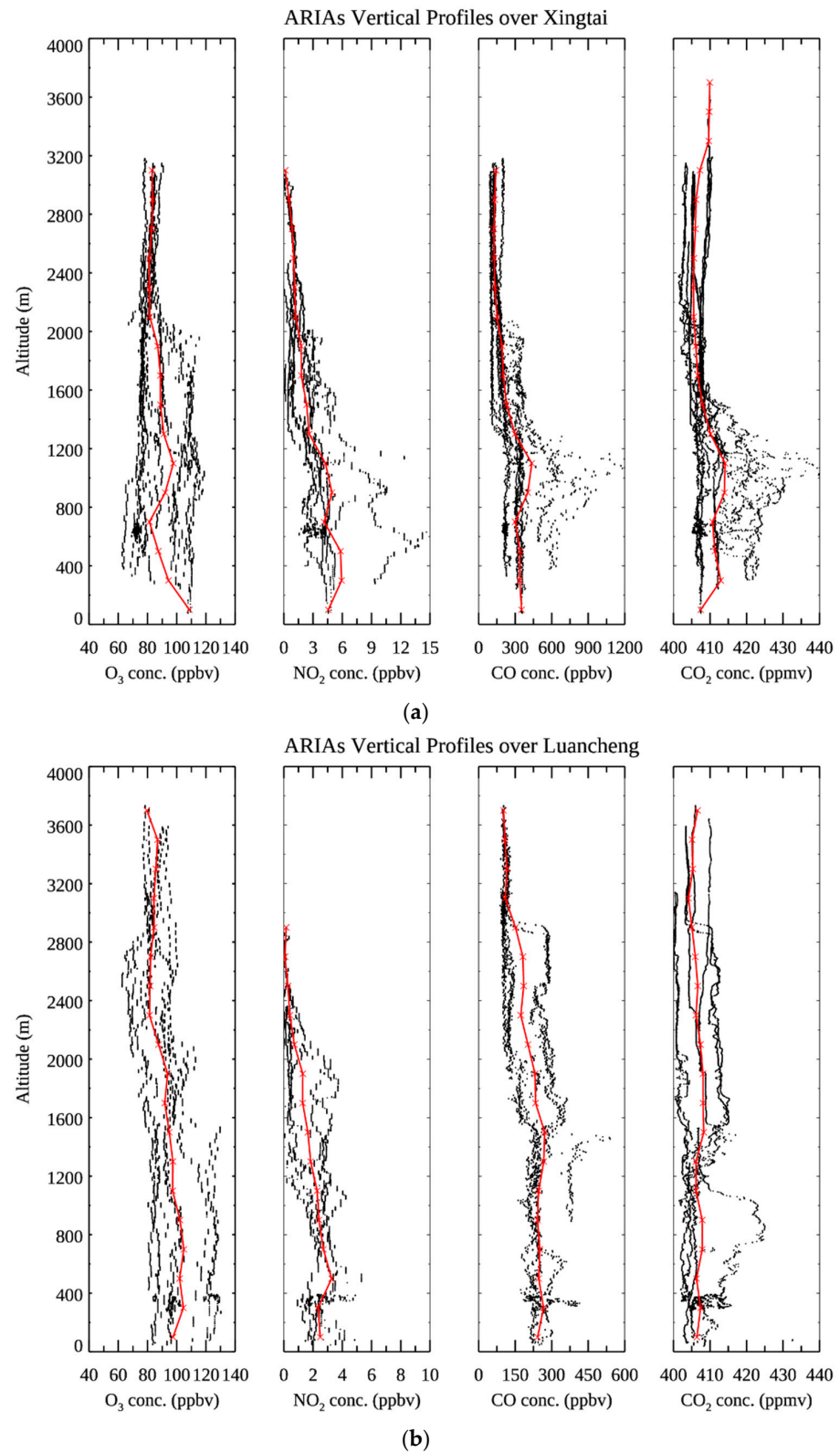

(**a**)

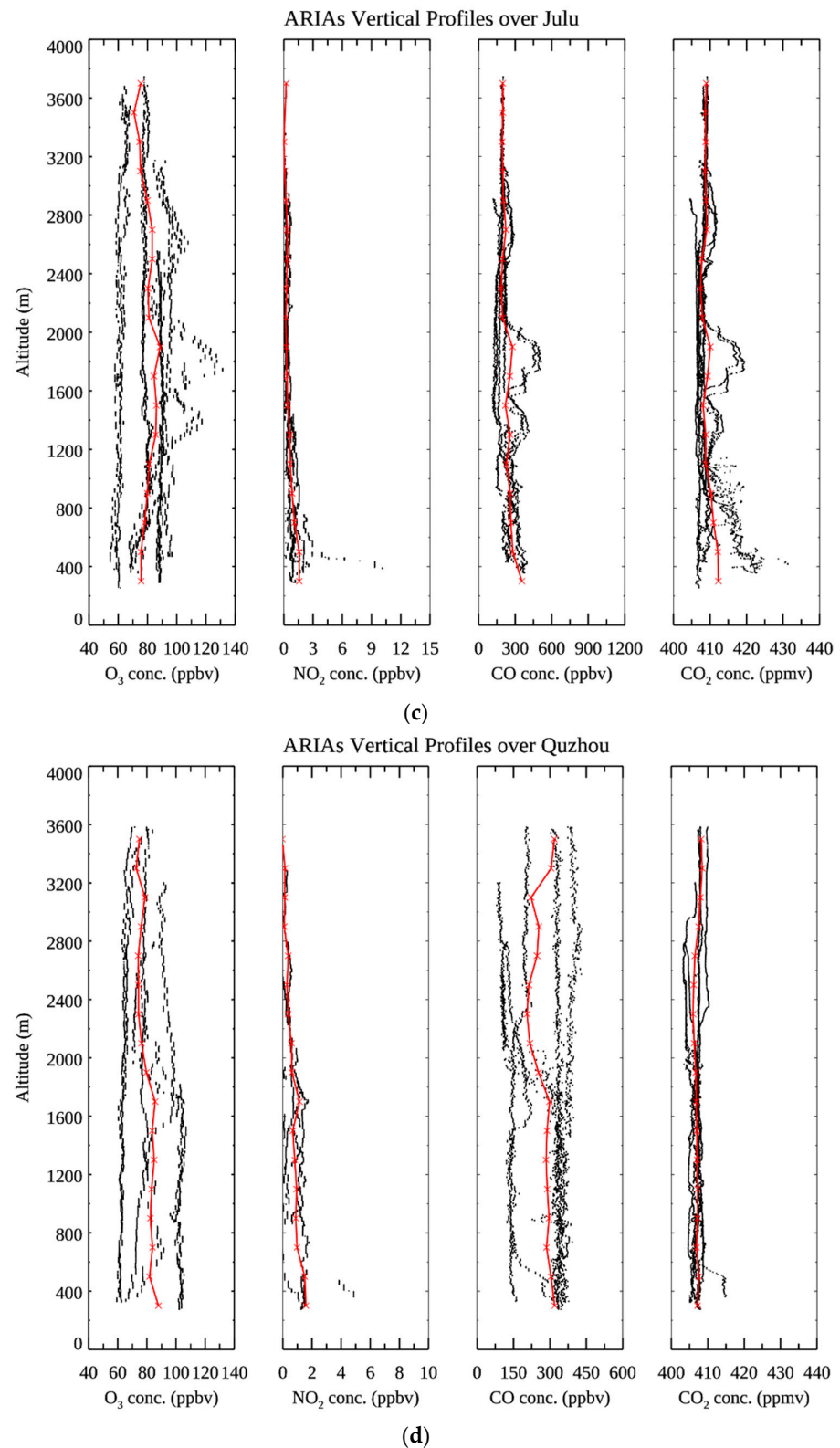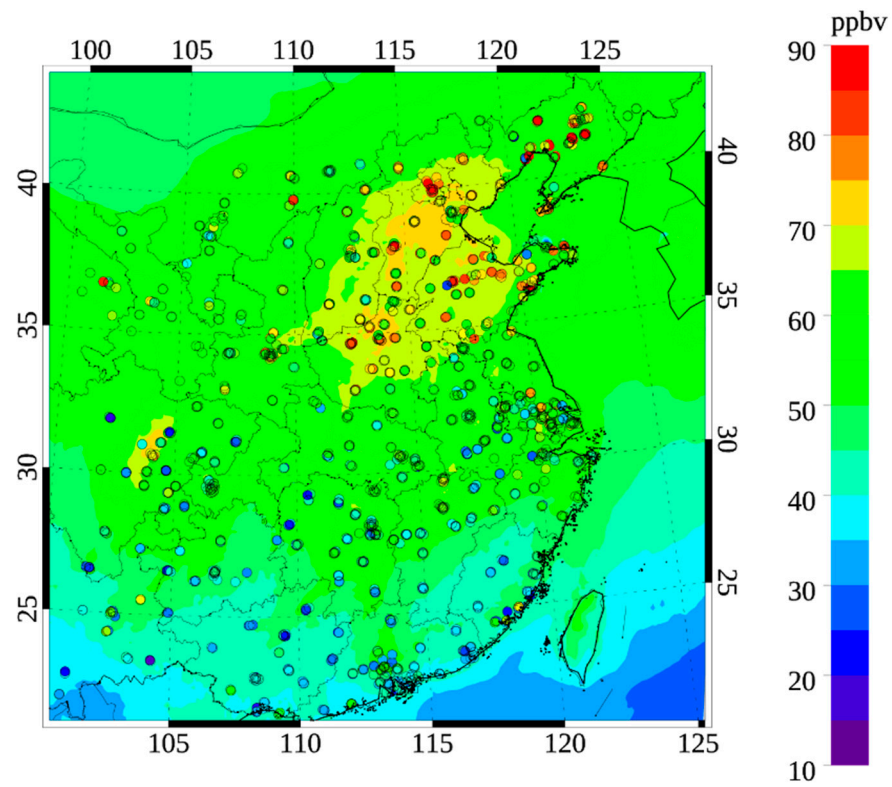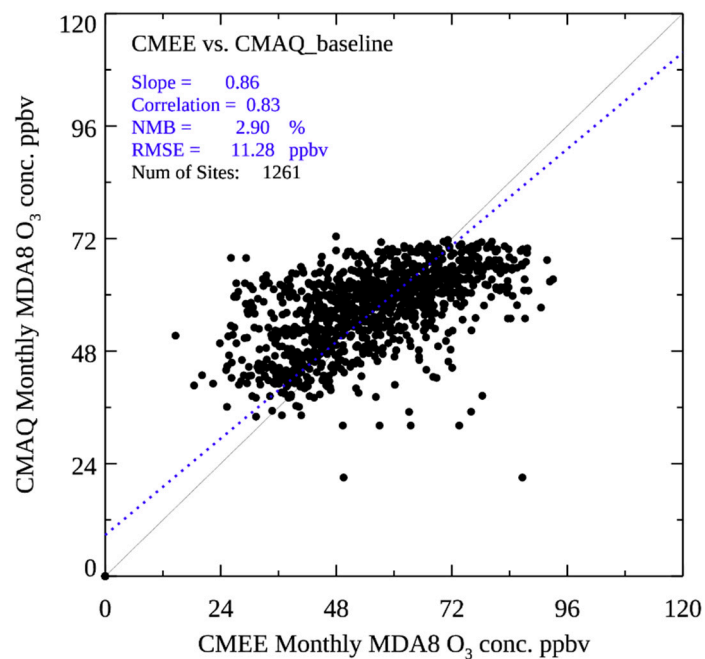(**b**)

Figure 3. *Cont.*

Figure 3. Vertical profiles of air pollutants over four locations in the NCP. (**a**) Xingtai (XT), (**b**) Luancheng (LC), (**c**) Julu (JL), and (**d**) Quzhou (QZ). Red lines show the mean profiles and red crosses represent the mean values averaged every 200 m.

(**a**)

(**b**)

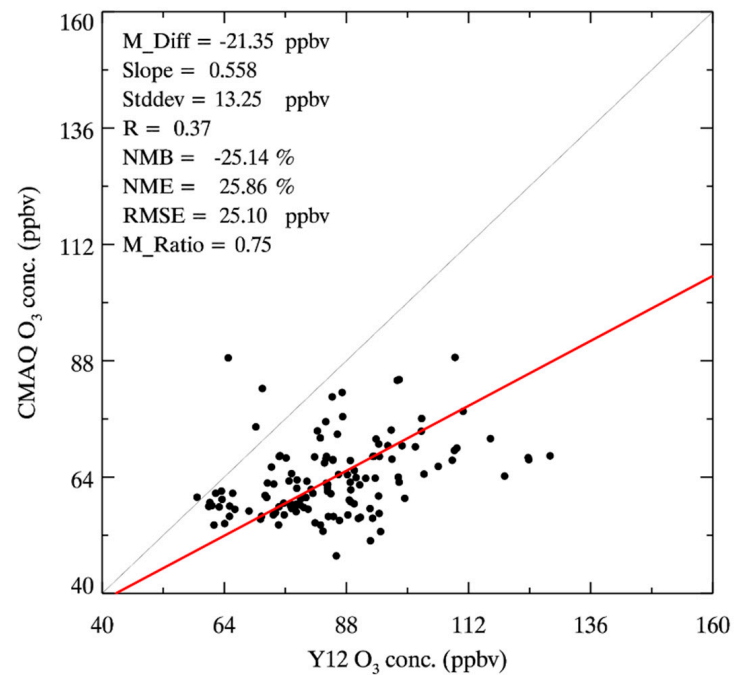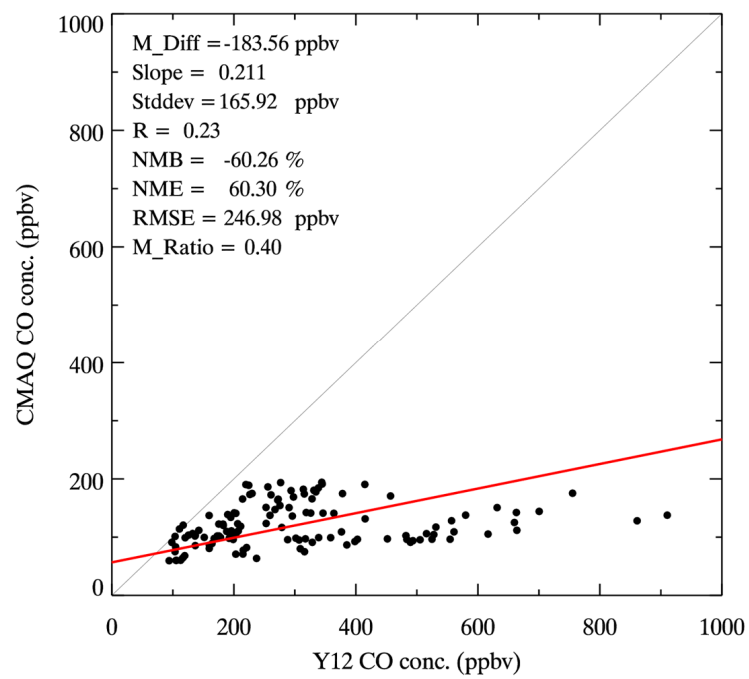**Figure 4.** Comparison of mean MDA8 ozone concentrations in May and June 2016 over eastern China. (**a**) Contour plot; the background stands for mean MDA8 ozone concentrations from the CMAQ_baseline run; the dots represent observed values from the CMEE network. (**b**) Scatter plot; blue line is the linear regression fitting.

(**a**)

(**b**)

Figure 5. *Cont.*

(**c**)

(**d**)

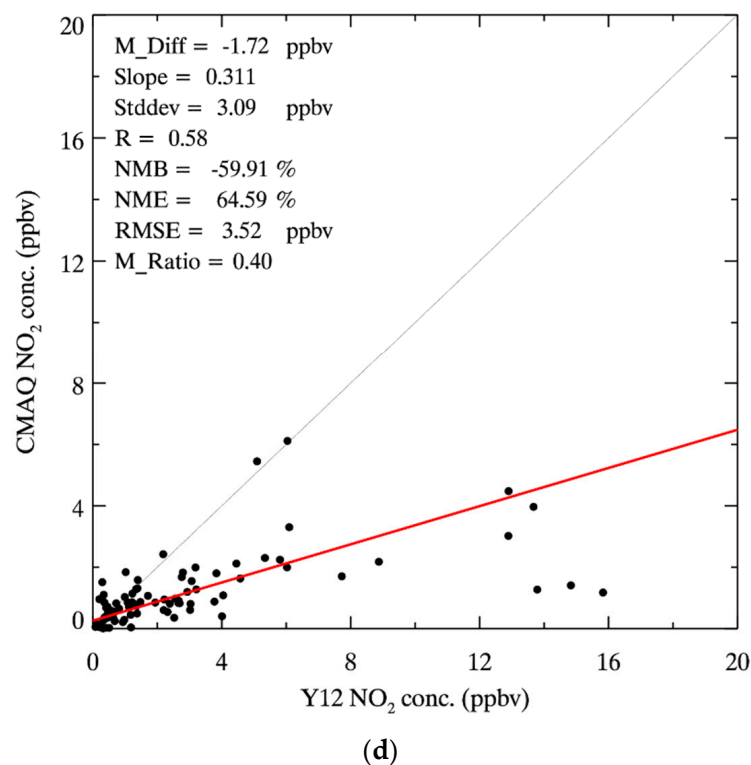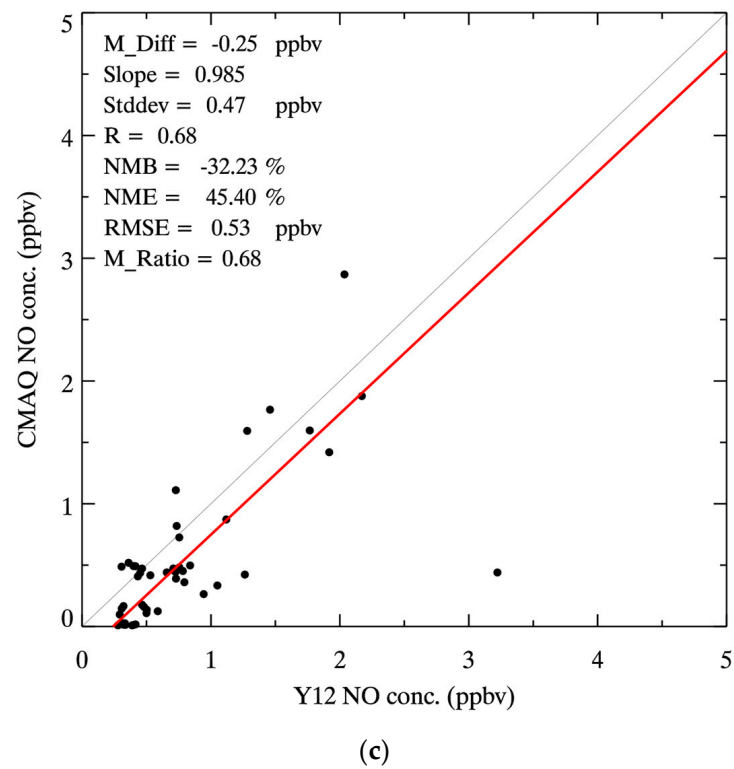**Figure 5.** Comparison of 10-minute averaged aircraft data and CMAQ simulations from 11 ARIAs research flights. (**a**) O$_3$, (**b**) CO, (**c**) NO, and (**d**) NO$_2$. Black line shows the 1:1 ratio; red line stands for the linear regression fitting line. M_Diff: mean difference; R: correlation; NMB: normalized mean bias; NME: normalized mean error; RMSE: root mean square error; M_Ratio: mean ratio.

Figure 6. Comparison of total VOC concentrations from WAS samples and CMAQ simulations. Values are in units of parts per billion Carbon (ppbC). Black line shows the 1:1 ratio; red line stands for the linear regression fitting line. M_Diff: mean difference; R: correlation; NMB: normalized mean bias; NME: normalized mean error; RMSE: root mean square error; M_Ratio: mean ratio.
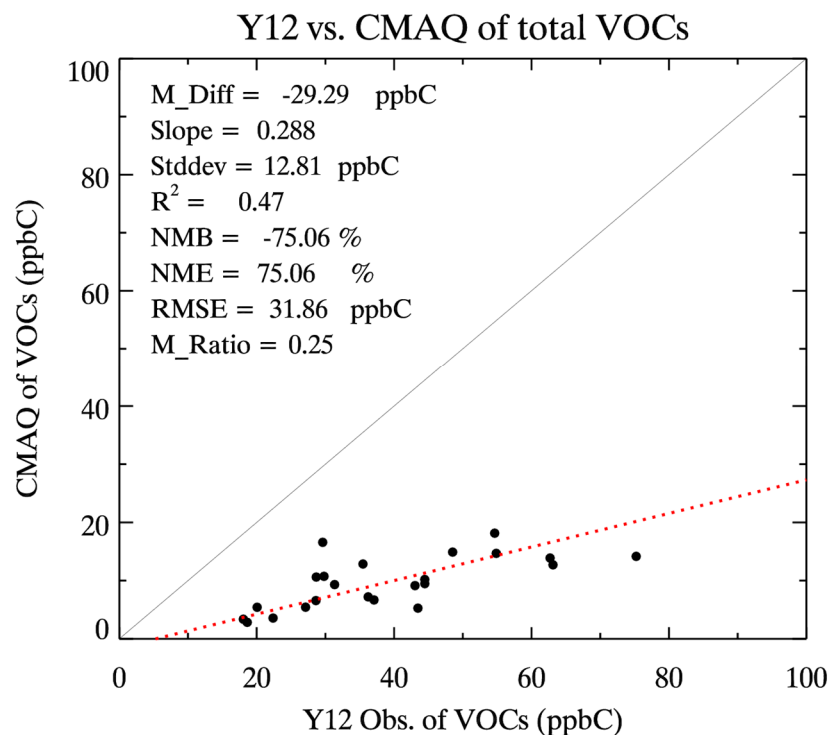
3.2. Evaluation of Emissions Inventory in the NCP

The EDGAR v4.2 emission inventory in East Asia was created based on the 2010 MIX emission inventory [129], so substantial changes were anticipated when used for the ARIAs campaign in 2016. Anthropogenic emission inventories are usually based on the "bottom-up" approach, which relies on the statistics of fossil fuel usage and emission factors (EFs) for each sector, defined as the ratio of the amount of air pollutants released by a unit of CO_2 emissions, e.g., CO/CO_2 and NO_x/CO_2. The 2010 EDGAR inventory has emissions for four sectors: Energy, Industry, Transportation, and Residential. We calculated the CO/CO_2, NO_x/CO_2, and NO_x/CO ratios through averaging the EFs from these four sectors (Figure 7).
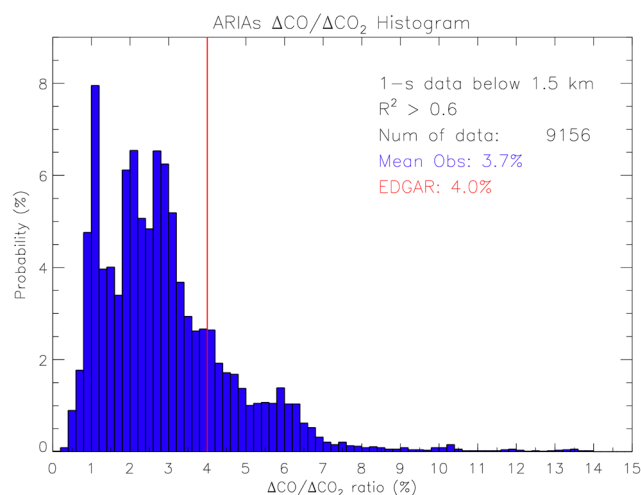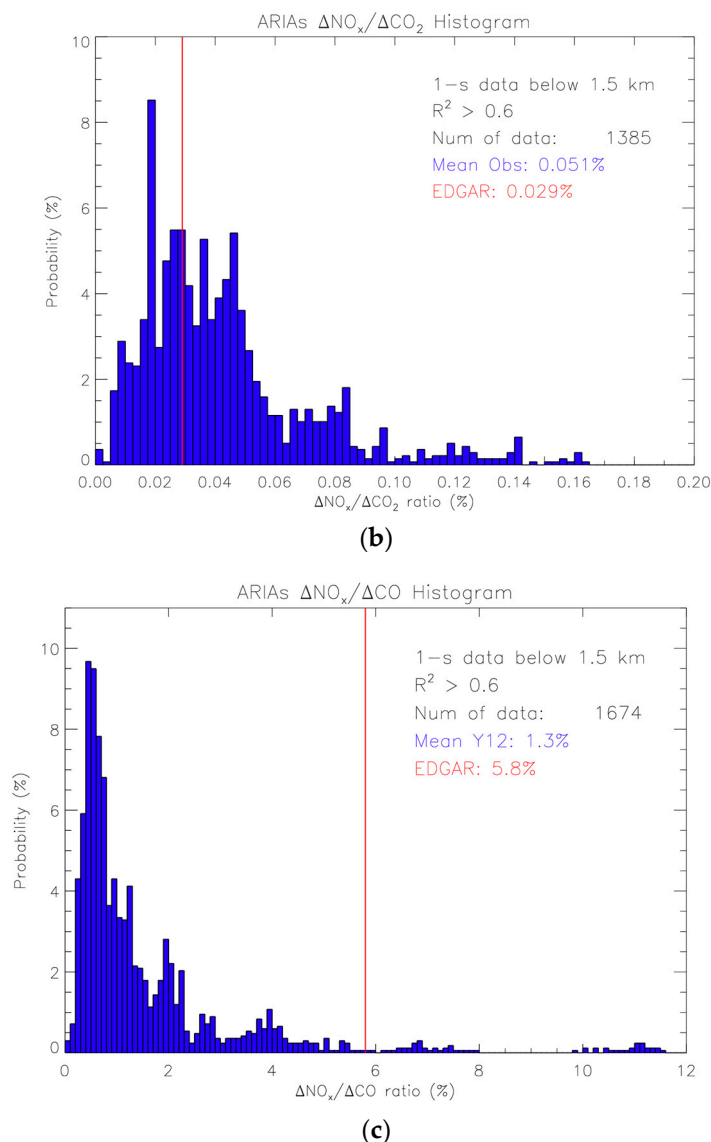

(**a**)

Figure 7. *Cont..*

Figure 7. Comparison of emission enhancements (EEs) from the ARIAs campaign and emission factors (EFs) from the EDGAR emission inventory. (**a**) $\Delta CO/\Delta CO_2$, (**b**) $\Delta NO_x/\Delta CO_2$, (**c**) $\Delta NO_x/\Delta CO$. Blue histogram shows the distribution of EEs observed by the Y12 aircraft; red line shows the ratio calculated through averaging EFs from four sectors of the EDGAR anthropogenic emissions inventory.

To evaluate the emission inventory data in the NCP, we used a plume recognition method to calculate the emission enhancements (EEs) from Y12 observations. We first selected 60 1-second aircraft measurements with a 60-second moving window. Then, we conducted linear regression of observed air pollutant (CO, NO_x, etc.) concentrations vs. CO_2 concentrations in each 60-second window and calculated the slope (i.e., $\Delta CO/\Delta CO_2$ and $\Delta NO_x/\Delta CO_2$) and correlation (R). The slope is defined as EEs in each window, standing for a 'plume' tested in the 60-second window. Lastly, we only selected EEs that were within the PBL (below 1.5 km AGL in this study) and statistically significant ($R^2 > 0.6$), so the values of these selected EEs could act as a proxy of EFs in the air mass observed. The detailed information about this plume recognition method can be found in Halliday et al. [87].

EEs observed during the research flights have a broad range of values. $\Delta CO/\Delta CO_2$ ranges from below 1%, a typical value of modern automobile emissions, to higher than 10%, a value indicating fossil fuel combustion with high emissions such as biomass burning (Figure 7a). The mean of observed EE for CO (3.7%) was close to that calculated from the EDGAR inventory (4.0%) in the aircraft campaign area. Observed $\Delta NO_x/\Delta CO_2$ ratios also

had isolated high values (>0.1%), with a mean value of 0.05%, which is substantially higher than the EF (~0.03%) derived from the EDGAR inventory (Figure 7b). Since estimation of anthropogenic CO_2 flux in an urban/suburban area is challenging [130,131], the underestimation of CO and NO_x in the NCP could be caused by either underestimated EFs or uncertainty in anthropogenic CO_2 emission data used in the 'bottom-up' approach.

To further investigate the characteristics of air pollutant emissions in the NCP, we conducted a similar analysis of $\Delta NO_x/\Delta CO$, which are usually co-emitted in combustion processes. Since around half of the CO and NO_x are from mobile sources in the EDGAR emission inventory, this ratio can approximately represent the emission characteristic of mobile sources in the NCP. The mean observed $\Delta NO_x/\Delta CO$ ratio was ~1.3%, significantly lower than the 5.8% based on the EDGAR emission inventory (Figure 7c). These results suggest that the EDGAR emission inventory substantially overestimates the ratios of NO_x/CO, while the automobile emissions over the NCP in 2016 have been greatly improved due to recent regulations, i.e., EDGAR overestimates the contribution from combustion with high emission factors. It is worth noting that we only evaluated the emission ratios (EEs or EFs) in the EDGAR inventory during the ARIAs campaign, while the underestimation of CO and NO_x emissions could be caused by inaccurate CO_2 emissions, which is beyond the scope of this study.

3.3. Evaluation of CO, NO_x, and VOC Emissions Using Satellite Data

Satellite observations are widely used to evaluate the anthropogenic emissions in East Asia, sometimes supplemented by model simulations, e.g., CO emissions using the MOPITT CO products [132,133], anthropogenic NO_x emissions using OMI NO_2 products [134–136], and VOC emissions using OMI HCHO products [137]. In this study, we used measurements from multiple satellite instruments to evaluate the CMAQ performance of NO_2, HCHO, and CO. Since NO_2 and HCHO can be treated as proxies of NO_x and VOC emissions, we can further improve the 2010 EDGAR emissions over the NCP based on satellite data.

We followed the approach developed in Canty et al. [138] to compare the tropospheric column contents of NO_2 from OMI products and CMAQ simulations. Level 2 OMI NO_2 swatch information including row anomaly and quality flags was used to sample NO_2 vertical profiles from CMAQ outputs, and then the CMAQ NO_2 column was calculated using the OMI averaging kernel (AK). Lastly, we averaged OMI and CMAQ NO_2 column contents to create daily $0.25° \times 0.25°$ Level 3 products (see details in [138]). A similar approach was used to integrate HCHO column contents from CMAQ simulations based on OMI HCHO retrievals (see details in [66]) and construct daily $0.25° \times 0.25°$ Level 3 HCHO products. For tropospheric CO, we selected the CO concentrations at ~900 hPa in CMAQ and averaged them to $1.0° \times 1.0°$ daily products using the MOPITT CO averaging kernel [102]. All gridded daily data of satellite and CMAQ were averaged in May and June 2016 for comparison.

We plotted OMI NO_2 columns in eastern China (Figure 8a), which showed strong signals over the NCP. NO_2 columns from OMI and CMAQ generally agreed well over eastern China, but large discrepancies existed in some regions (Figure 9a). For the aircraft campaign area, CMAQ underestimates NO_2 columns (slope = 0.95 and mean ratio = 0.81, i.e., only predicts 81% of OMI NO_2 column) with uncertainties relatively smaller within the campaign period (Figure 9b). However, in urban regions such as Beijing, the Yangtze River Delta (YRD), and the PRD, CMAQ substantially overestimates column NO_2 by up to 30% (Figure 8a). Because the CMAQ_baseline run used the 2010 anthropogenic emission data, these differences should represent the changes in NO_x emissions due to recent air pollution regulations. The comparison of NO_2 columns suggests that NO_x pollution of megacities in China has been substantially improved since 2010, while NO_x pollution in smaller cities and rural area has worsened, consistent with results from independent studies using OMI products [57,139]. OMI HCHO retrievals also show high values over the NCP in spring, when plants' photosynthetic activity is relatively low, reflecting the dominance of anthropogenic VOC emissions in northern China [61,140]. CMAQ has good agreement

with OMI HCHO within the aircraft campaign area (<20% underestimation), but substantially underestimates HCHO columns in southern China, where biogenic VOC emissions dominate (Figure 8b). The MOPPIT products show high near-surface CO concentrations over eastern China (Figure 8c), while the CMAQ_baseline run substantially underestimates CO over northern China and only predicts 42% of the CO over the aircraft campaign area.

(**a**)

(**b**)

(**c**)
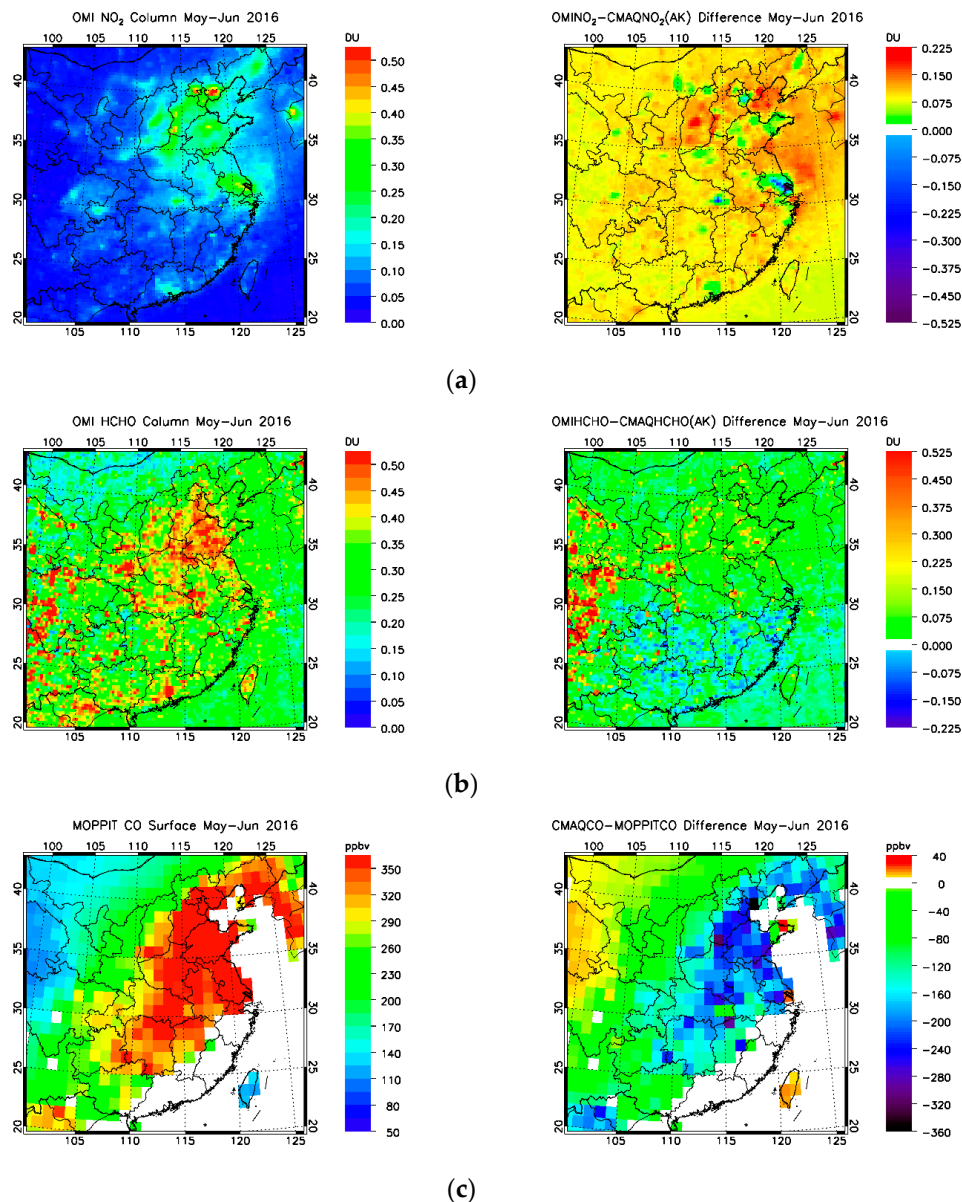
Figure 8. Comparison of air pollutants from satellite observations and CMAQ simulations. (**a**) OMI NO_2 column (**left**) and the difference between OMI and CMAQ (**right**), Unit: Dobson Unit (1 DU = 2.69×10^{20} molecules/cm^2). (**b**) OMI HCHO column (**left**) and the difference between OMI and CMAQ (**right**), Unit: DU. (**c**) MOPITT near-surface CO (**left**) and the difference between MOPITT and CMAQ (**right**), Unit: ppbv.
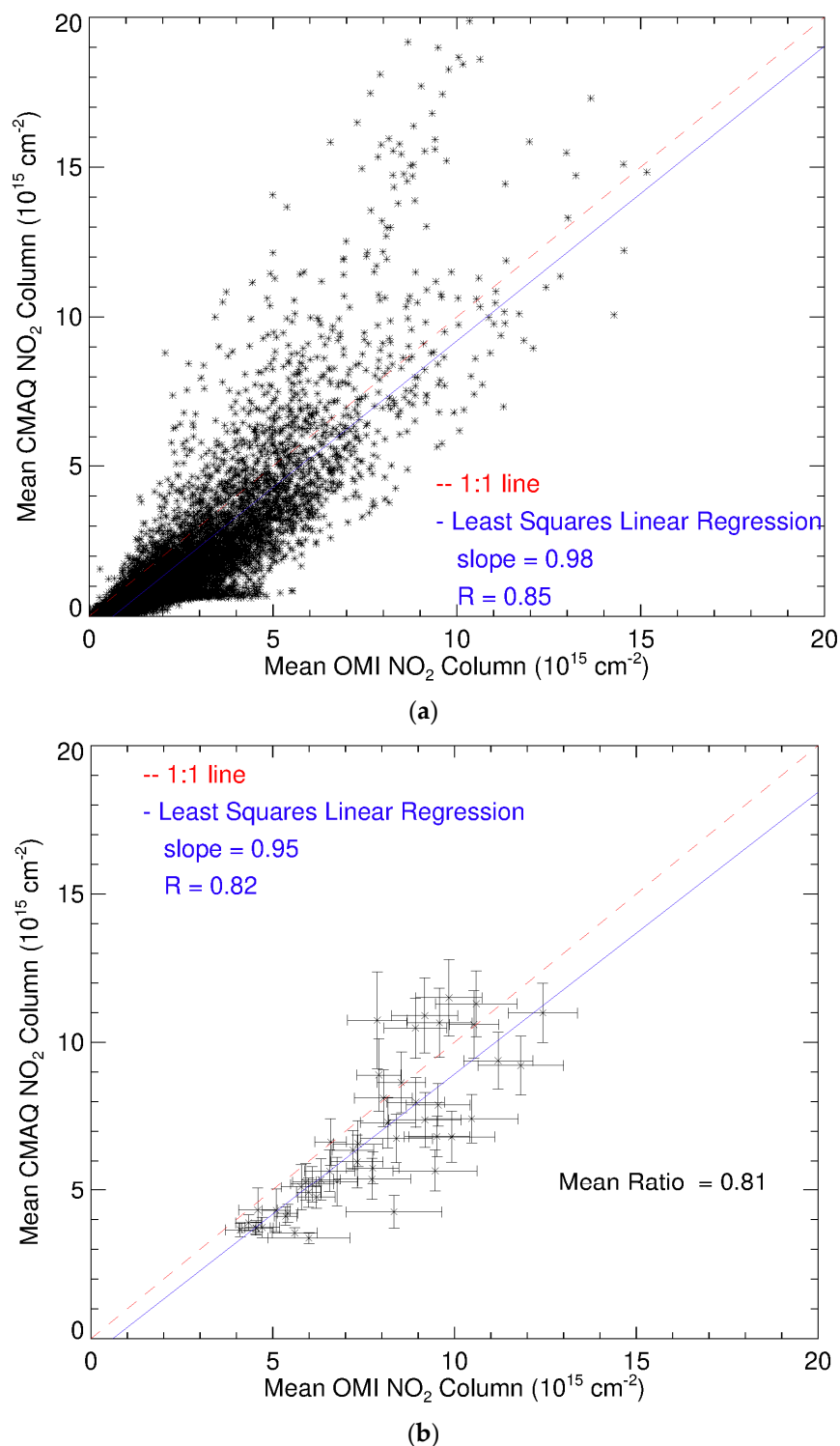
Figure 9. Comparison of OMI NO_2 and CMAQ NO_2 columns averaged in May and June 2016. (**a**) Scatter plot of NO_2 columns over eastern China. (**b**) Scatter plot of NO_2 columns over the campaign area (error bars were calculated as the standard deviation of daily OMI products and daily CMAQ simulations during the 2-month campaign).

Using NO_2 and HCHO as proxies of NO_x and VOC emissions, the comparison of satellite observations and the CMAQ_baseline simulations suggests that both NO_x and VOC emissions in the aircraft campaign area need to be adjusted for a better simulation of tropospheric ozone. Also, the underestimation of CO, as an important precursor, can lead to underprediction of tropospheric ozone. We calculated the model/satellite ratios of NO_x,

HCHO, and CO in East Asia (Figure S6 in the Supplementary Materials) and used these ratios to adjust their anthropogenic emissions in CMAQ. The results will be discussed in Section 3.5.

3.4. Tropospheric Ozone Production Sensitivity from OMI and CMAQ

Photochemical production of tropospheric ozone is highly non-linear and dependent on concentrations of NO_x and VOCs [64,141,142]. A maximum rate of ozone production can be achieved with an optimal VOCs/NO_x ratio. With other VOCs/NO_x ratios, ozone production can be either in the VOC-sensitive regime (the rate of ozone production is controlled by VOC concentrations) or in the NO_x-sensitive regime (the rate of production is controlled by NO_x concentrations). Different pollution control strategies can be implemented to reduce the tropospheric ozone levels in these two regimes. For instance, in a VOC-sensitive environment, reducing NO_x emissions will lead to limited effects until the ozone production has been changed to a NO_x-sensitive environment with the continuous removal of NO_x from the atmosphere. Duncan et al. [65] developed an approach using the OMI HCHO/NO_2 column ratio to estimate the ozone production sensitivity as follows: (1) HCHO/NO_2 < 1: VOC-sensitive regime; (2) HCHO/NO_2 1~2: transition regime; (3) HCHO/NO_2 > 2: NO_x-sensitive regime. Studies show that urban areas in the U.S. such as Los Angeles, New York City and Houston are in VOC-sensitive or transition regimes, which lead to difficulty in local regulation of air quality [65,66,121]. Recent studies suggest new threshold values of HCHO/NO_2 ratios between VOC-sensitive, transition, and NO_x-sensitive regimes in the U.S. [67,143].

Using the Duncan et al. [65] approach, results from OMI products suggest large areas of eastern China are either in a VOC-sensitive regime (mostly megacities such as Beijing) or in a transition regime [67,68,144]. We followed the approach described in Ring et al. [66] to calculate the column HCHO/NO_2 ratios from OMI observations and CMAQ simulations for East Asia. OMI column HCHO/NO_2 ratios suggest that the ozone photochemical production is in a VOC-sensitive or transition regime over the NCP and other major urban areas such as YRD and PRD (Figure 10a) if the Duncan et al. [65] approach is applicable for these areas. CMAQ successfully captured the spatial distribution of the regional nature of ozone production sensitivity in eastern China but predicted that the rate of ozone production is controlled more by VOCs with the CMAQ HCHO/NO_2 ratio lower than 1.0 in Beijing, YRD, and PRD (Figure 10b). The VOC-sensitive environment from both OMI observations and CMAQ simulations suggests the rate of ozone photochemical production in the NCP is controlled not only by NO_x emissions, but also by VOC emissions, for which regulations are currently lacking in China. With continuous reduction of anthropogenic NO_x emissions in China, VOC controls might be efficient in these VOC-sensitive regions.

3.5. Improvements in Tropospheric Ozone Simulation Using Satellite Products

Results of the previous two sections show that the CMAQ_baseline run substantially underestimates the concentrations of ozone and its major precursors in the NCP. Independent studies using KORUS-AQ observations and satellite products suggested that major ozone precursor emissions such as CO and NO_x could have large discrepancies as compared with emission inventory in East Asia [145,146]. To identify the individual and combined effects of emission discrepancies for major ozone precursors in the NCP, we designed a series of sensitivity experiments with emissions adjusted to satellite observations. Unlike the top-down approach using global chemical transport models such as GEOS-Chem [135,147], here we simply applied the ratios of air pollutant column contents from satellite observations and CMAQ simulations on each 0.25 degree grid (Figure S6 in the Supplementary Materials) as CO_{CMAQ}/CO_{MOPITT}, NO_{2CMAQ}/NO_{2OMI}, and $HCHO_{CMAQ}/HCHO_{OMI}$ ratios for anthropogenic CO, NO_x, and VOC emissions, respectively. To estimate the contribution from biogenic VOC emissions, we conducted one more run with the in-line BEIS module turned off.
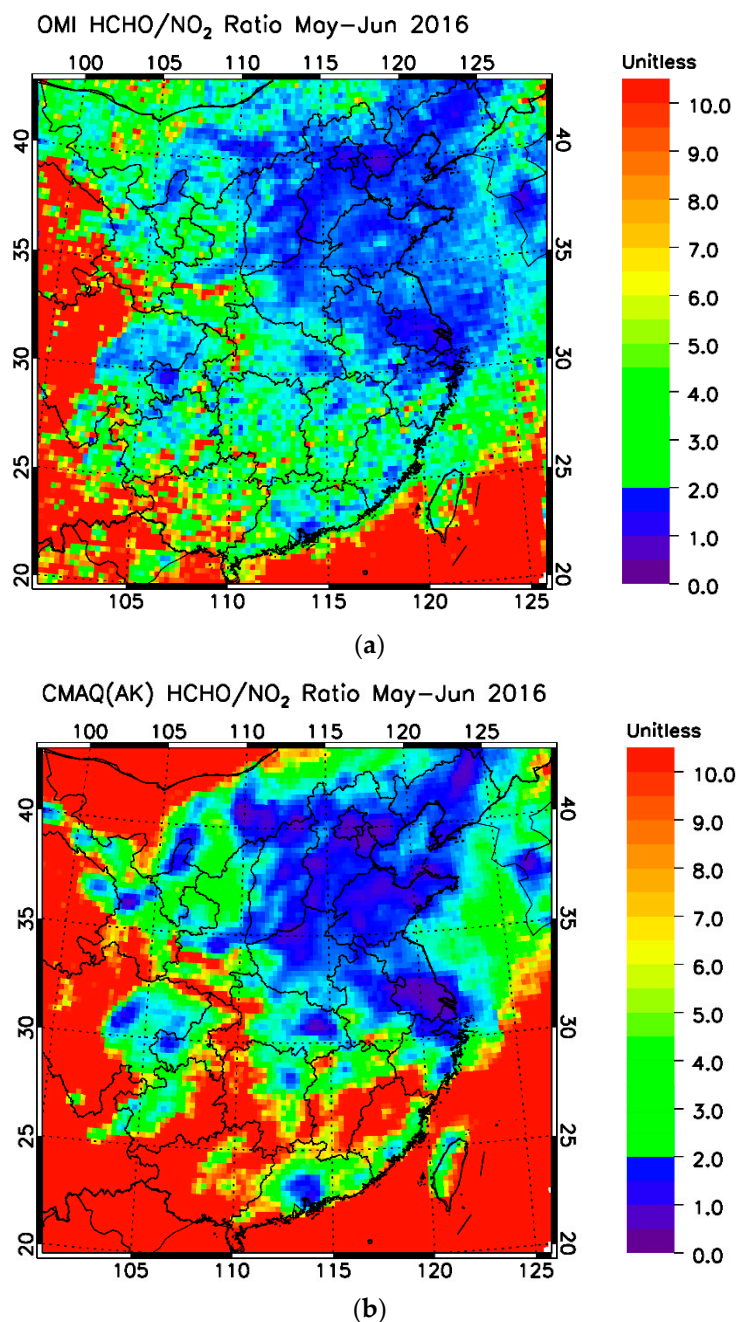
Figure 10. Column HCHO/NO$_2$ ratios over East Asia in 2016. (**a**) Ratio derived from collocated OMI HCHO and NO$_2$ observation. (**b**) Ratio calculated from CMAQ HCHO and NO$_2$ simulations with OMI quality information and averaging kernel (AK).

Table 1 shows the emission adjustments for the five sensitivity experiments. CMAQ was run for the nested 12 km domain (D02) with the same meteorology, initial conditions, and boundary conditions derived from the coarse domain results of the CMAQ_baseline run. We conducted a similar analysis of Figure 8 to investigate the discrepancy between satellite products and CMAQ simulations over eastern China (Figure S7 in the Supplementary Materials). The CMAQ_all run successfully reproduced the column NO$_2$ and near-surface CO in eastern China and column HCHO in the NCP. In southern China, where biogenic VOCs dominate, adjusting anthropogenic VOC emissions showed limited improvements on column HCHO simulations.

Table 1. List of CMAQ simulations with adjusted emissions based on satellite observations. Anthropogenic NO_x, VOC, and CO emissions were adjusted using OMI NO_2, OMI HCHO, and MOPITT CO, observations.

Run NO.	Experiment Name	Bio. VOCs	Anthro. CO	Anthro. NO_x	Anthro. VOCs
1	CMAQ_baseline	BEIS	EDGAR	EDGAR	EDGAR
2	CMAQ_noBEIS	N/A	EDGAR	EDGAR	EDGAR
3	CMAQ_NO_x	BEIS	EDGAR	Adjusted	EDGAR
4	CMAQ_VOCs	BEIS	EDGAR	Adjusted	EDGAR
5	CMAQ_CO	BEIS	Adjusted	EDGAR	EDGAR
6	CMAQ_All	BEIS	Adjusted	Adjusted	Adjusted

Figure 11 compares the mean MDA8 ozone concentrations from CMEE observations and the CMAQ_all run, and similar analyses for the other four CMAQ sensitivity experiments are presented in Figure S8 of the Supplementary Materials. CMAQ sensitivity experiments driven by modified emissions showed better results in simulating the surface ozone in eastern China, while the CMAQ_all run has successfully produced the high surface ozone in the NCP. In Table 2, we summarize the statistics from linear regression analyses of CMEE observations and all CMAQ sensitivity experiments in eastern China. Generally, the adjustment of anthropogenic emissions has improved CMAQ simulations of O_3, CO, and NO_2. Improvements in surface ozone simulations are sensitive to adjustments of both NO_x and VOC emissions; improvements in modeled CO are only sensitive to the adjustment of CO emissions; improvements in surface NO_2 results are sensitive to VOC emission adjustments. These results are consistent with our previous conclusion that the VOC-sensitive environment dominates in eastern China.
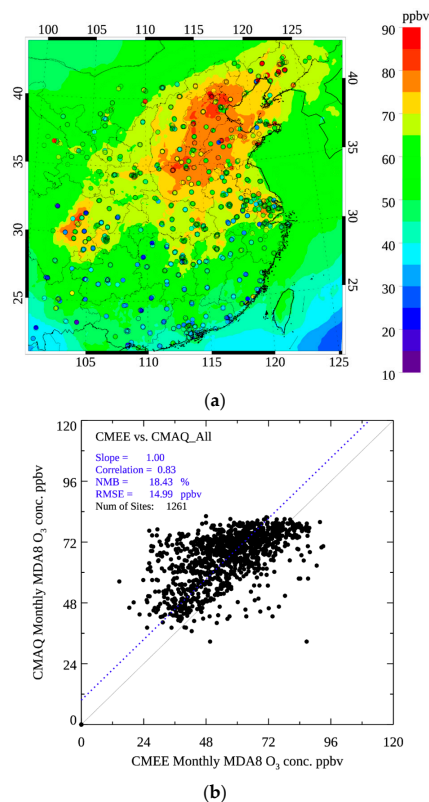

(**a**)

(**b**)

Figure 11. Similar to Figure 4, but compares MDA8 ozone concentrations from CMEE observations and the CMAQ_all run. (**a**) Contour plot; the background stands for mean MDA8 ozone concentrations from the CMAQ_baseline run; the dots represent observed values from the CMEE network. (**b**) Scatter plot; blue line is the linear regression fitting.
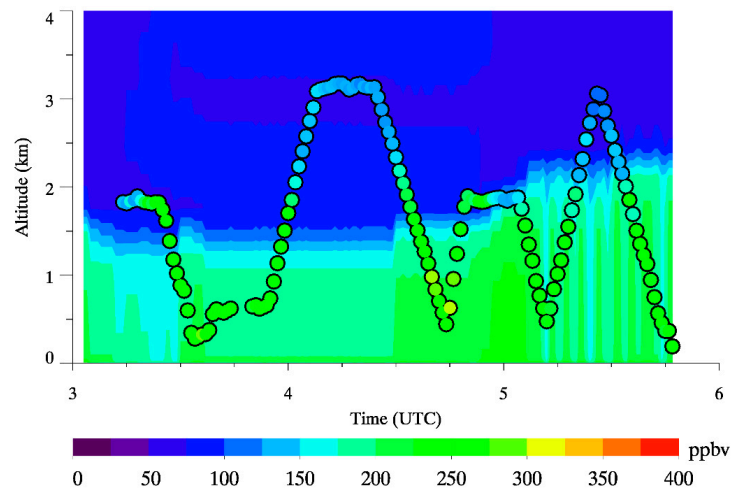
Table 2. Statistics of CMAQ performance in six sensitivity experiments compared with CMEE observations in eastern China. Slope and Correlation R (Corr. R) are from the linear regression analysis; NMB = normalized mean bias; RMSE = root mean square error.

| No.	Name	Slope	Corr. R	NMB	RMSE
		Unitless	Unitless	%	ppbv
		O_3			
1	CMAQ_Baseline	0.86	0.83	2.90	11.28
2	CMAQ_noBEIS	0.79	0.83	−4.44	11.30
3	CMAQ_NO$_x$	0.92	0.81	11.66	13.27
4	CMAQ_VOCs	0.91	0.84	7.12	11.40
5	CMAQ_CO	0.88	0.83	5.00	11.46
6	CMAQ_All	1.00	0.83	18.43	14.99
		CO			
1	CMAQ_Baseline	0.40	0.33	−72.53	551.34
2	CMAQ_noBEIS	0.39	0.32	−73.39	556.65
3	CMAQ_NO$_x$	0.40	0.32	−72.70	552.35
4	CMAQ_VOCs	0.40	0.33	−72.32	550.07
5	CMAQ_CO	0.65	0.30	−62.76	510.28
6	CMAQ_All	0.65	0.30	−62.75	510.25
		NO_2			
1	CMAQ_Baseline	0.93	0.45	−54.72	9.06
2	CMAQ_noBEIS	0.92	0.45	−56.82	9.22
3	CMAQ_NO$_x$	0.81	0.45	−52.30	8.65
4	CMAQ_VOCs	0.96	0.44	−54.85	9.18
5	CMAQ_CO	0.93	0.45	−54.68	9.08
6	CMAQ_All	0.84	0.43	−52.52	8.79

The ARIAs flights covered a large area (~10^4 km^2) in Hebei Province representing the regional nature of air pollution over the NCP. A case comparison of CMAQ_All run and Y12 measurements on 11 June 2016 (Figure 12) showed better results in both concentrations and vertical gradient of air pollutants (compared with Figure S5 in the Supplementary Materials), indicating the effectiveness of improving the emission inventories based on satellite observations. Table 3 summarizes the model performance of CMAQ as compared with aircraft measurements, and scatter plots for each CMAQ sensitivity experiment are shown in Figure S9 of the Supplementary Materials. The adjustments of the EDGAR emissions with satellite observations substantially improved simulations of ozone pollution, with the root mean square error (RSME) decreasing from 25.1 ppbv (the CMAQ_baseline run) to 21.2 ppbv (the CMAQ_All run), and the mean ratio of CMAQ simulations to aircraft observations increasing from 0.75 to 0.82. The model performance of CO has also been improved, with the RMSE decreasing from 247.0 ppbv to 203.6 ppbv, and the mean ratio increasing from 0.40 to 0.66. For nitrogen compounds including NO_2, NO, and NO_y, the adjustments of EDGAR emissions had small impacts on improving the CMAQ performance. The reason could be that the ozone photochemistry is mainly VOC-sensitive over the NCP, so the adjustments of NO_x emissions have limited impacts close to sources.
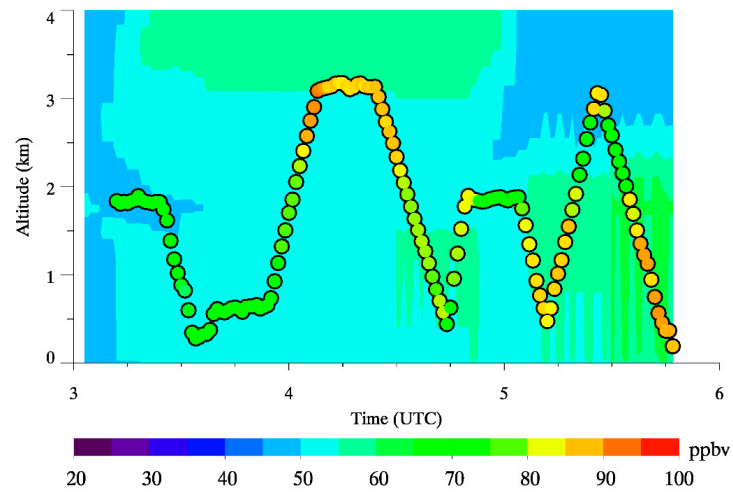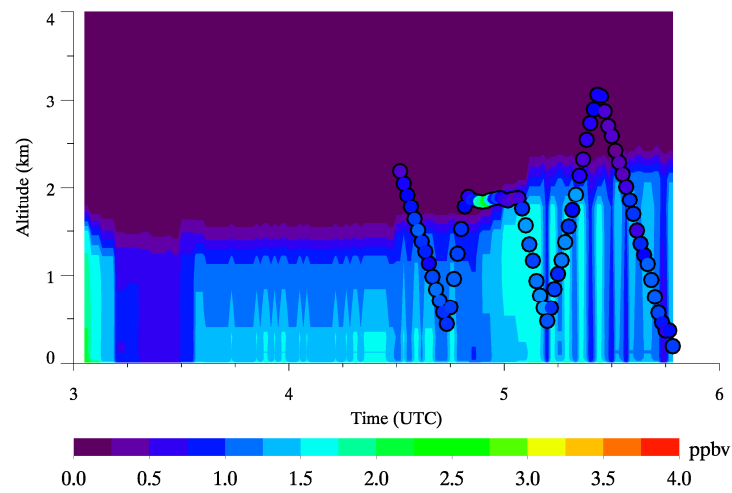
(**a**)

(**b**)
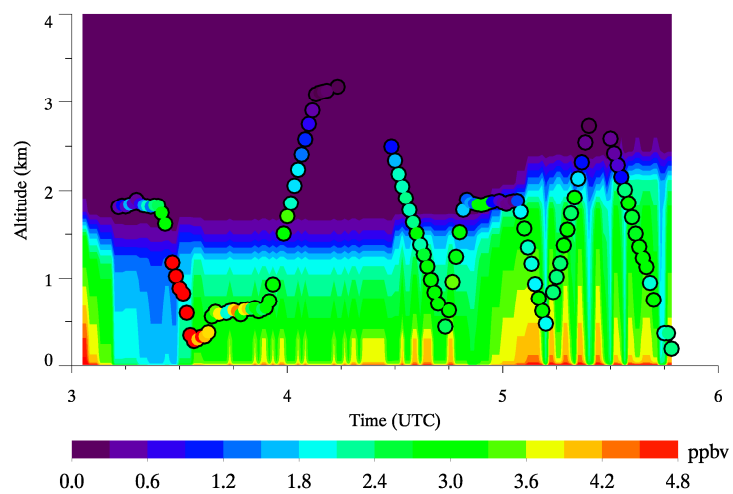
(**c**)

Figure 12. *Cont.*

(**d**)
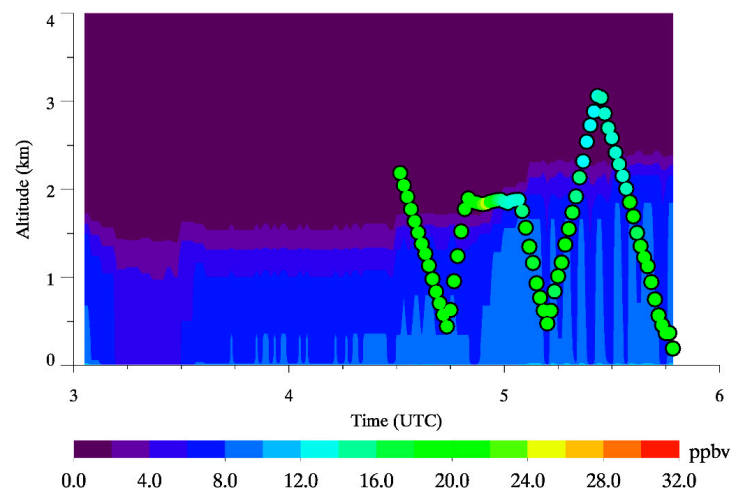
(**e**)

Figure 12. A case study comparing aircraft observations and the CMAQ_All run results on June 11, 2016. Background: CMAQ simulations. Overlay: 1 min Y12 measurements. (**a**) O_3, (**b**) CO, (**c**) NO_2, (**d**) NO, and (**e**) NO_y.

Table 3. Statistics of CMAQ performance in six sensitivity experiments compared with ARIAs aircraft measurements over the NCP.

No.	Name	Mean Diff	Slope	Stdev	Corr. R	NMB	NME	RMSE	Mean Ratio
		ppbv	Unitless	ppbv	Unitless	%	%	ppbv	Unitless
					O_3				
1	CMAQ_Baseline	−21.35	0.56	13.25	0.37	−25.14	25.86	25.10	0.75
2	CMAQ_noBEIS	−23.74	0.49	12.85	0.41	−27.94	28.34	26.97	0.72
3	CMAQ_NO$_x$	−19.83	0.59	13.63	0.34	−23.34	24.18	24.03	0.77
4	CMAQ_VOCs	−19.26	0.66	13.66	0.36	−22.67	23.81	23.58	0.77
5	CMAQ_CO	−20.35	0.61	13.52	0.36	−23.96	24.83	24.40	0.76
6	CMAQ_All	−15.18	0.81	14.83	0.33	−17.87	20.33	21.18	0.82

Table 3. *Cont.*

No.	Name	Mean Diff	Slope	Stdev	Corr. R	NMB	NME	RMSE	Mean Ratio
		ppbv	Unitless	ppbv	Unitless	%	%	ppbv	Unitless
				CO					
1	CMAQ_Baseline	−183.56	0.21	165.92	0.23	−60.26	60.26	246.98	0.40
2	CMAQ_noBEIS	−186.34	0.21	165.52	0.25	−61.17	61.17	248.79	0.39
3	CMAQ_NO$_x$	−184.25	0.21	165.76	0.24	−60.48	60.50	247.39	0.40
4	CMAQ_VOCs	−181.89	0.22	166.32	0.22	−59.71	59.78	246.01	0.40
5	CMAQ_CO	−148.55	0.36	167.90	0.22	−48.76	50.32	223.67	0.51
6	CMAQ_All	−104.45	0.52	175.48	0.21	−34.29	45.03	203.60	0.66
				NO$_2$					
1	CMAQ_Baseline	−1.72	0.31	3.09	0.58	−59.91	64.59	3.52	0.40
2	CMAQ_noBEIS	−1.73	0.31	3.09	0.58	−60.47	64.90	3.52	0.40
3	CMAQ_NO$_x$	−1.45	0.38	2.99	0.60	−50.61	61.26	3.31	0.49
4	CMAQ_VOCs	−1.76	0.31	3.10	0.58	−61.60	65.66	3.55	0.38
5	CMAQ_CO	−1.70	0.31	3.09	0.58	−59.28	64.20	3.51	0.41
6	CMAQ_All	−1.47	0.38	3.01	0.59	−51.23	61.62	3.33	0.49
				NO					
1	CMAQ_Baseline	−0.25	0.99	0.47	0.68	−32.23	45.4	0.53	0.68
2	CMAQ_noBEIS	−0.24	1.02	0.48	0.68	−31.09	45.66	0.54	0.69
3	CMAQ_NO$_x$	−0.08	1.31	0.59	0.67	−9.75	50.01	0.59	0.90
4	CMAQ_VOCs	−0.30	0.89	0.45	0.68	−38.63	46.58	0.54	0.61
5	CMAQ_CO	−0.26	0.96	0.47	0.68	−33.08	45.26	0.53	0.67
6	CMAQ_All	−0.16	1.13	0.52	0.67	−20.31	45.46	0.54	0.80
				NO$_y$					
1	CMAQ_Baseline	−15.26	0.30	10.15	0.39	−77.58	77.58	18.27	0.22
2	CMAQ_noBEIS	−15.50	0.29	10.15	0.40	−78.81	78.81	18.47	0.21
3	CMAQ_NO$_x$	−14.24	0.37	10.20	0.37	−72.39	72.39	17.46	0.28
4	CMAQ_VOCs	−15.23	0.30	10.16	0.39	−77.42	77.42	18.25	0.23
5	CMAQ_CO	−15.26	0.30	10.15	0.39	−77.56	77.56	18.27	0.22
6	CMAQ_All	−14.21	0.37	10.20	0.37	−72.26	72.26	17.44	0.28

4. Conclusions and Discussion

The ARIAs campaign conducted aircraft measurements over the NCP and observed high concentrations of air pollutants, including O_3, CO, and nitrogen compounds. CMAQ simulations driven by the 2010 EDGAR emissions substantially underestimated levels of ozone and its precursors in the campaign region. Analysis of emission enhancements of CO and NO_x with respect to concurrent CO_2 measurements suggested that the usage of the 2010 EDGAR emissions for the 2016 ARIAs campaign could introduce substantial uncertainty due to the recent changes in anthropogenic emissions in China. Comparison of atmospheric columns of NO_2 from CMAQ simulations and satellite observations showed that NO_x emissions decreased in megacities such as Beijing and Shanghai but increased in rural areas from 2010 to 2016. Similar analysis of HCHO and CO showed that the EDGAR VOC and CO emissions could be also underestimated in the NCP. The HCHO/NO_2 column ratio from OMI observations indicated tropospheric ozone production was mainly in the VOC-sensitive regime in the NCP, which was also confirmed by CMAQ simulations. To improve the model performance, we adjusted the EDGAR emissions over East Asia based on satellite observations. Better performance in simulating ozone and its precursors was achieved, as compared with surface and airborne observations.

The ARIAs aircraft measurements revealed substantial amounts of tropospheric ozone observed in the free troposphere (i.e., >80 ppbv with 2–3 km AGL in Figure 2), which agrees with the global studies [148–152]. The high ozone concentrations aloft can be transported for a long distance and mixed downwind through the PBL development to impact surface ozone concentrations, as we observed in the U.S. [97]. Our modeling approach used the default built-in profiles as boundary conditions, so the transport from regions outside China was not taken into consideration, which might have overestimated the local photochemical production of ozone in the NCP. A more rigorous modeling study using dynamic boundary conditions downscaled from a global chemical transport model and advanced numerical tools such as the source apportionment technique is needed for future studies.

In the NCP, stratospheric intrusions could also have an important effect on surface ozone, with a typical enhancement of 20 ppbv [153]. Our aircraft measurements did not observe high ozone events with low CO concentrations (Figure 3), which are used as an indicator of stratospheric intrusions to the surface (SITS). However, due to limited flights within the 2-month campaign, these SITS could be missed by the research flights. The CMAQ model used in this study does not have the stratospheric chemistry component, so the potential impacts from the ozone-rich stratospheric airmass on the surface ozone were also not simulated.

Recent reports [154] suggest that emissions of nitrous acid (HONO) from fertilized soils can contribute to ozone formation. The version of CMAQ used in this study does not consider this source, so inclusion of this process could further increase ozone production rates and sensitivity to VOCs in rural areas.

Both satellite observations and CMAQ simulations indicate that the VOC-sensitive chemistry dominates the ozone photochemical production in eastern China, so the rate of local ozone production is mainly controlled by the VOC emissions. In the past few years, despite implementation of control measures mainly on SO_2 and NO_x, ozone concentrations have increased in China. Our study indicated that high NO_x concentrations were pervasive in the PBL over rural areas of the NCP, where anthropogenic VOCs were also abundant. Reducing NOx emissions is essential to control ozone on the regional scale, but our model simulations indicated that reducing VOC emissions can lower the rate of photochemical smog production.

Currently, studies and regulations on anthropogenic VOC emissions are lacking, so with the expectation of further decreasing NO_x emissions in China, more severe ozone pollution could be anticipated. Even though hydrocarbon controls can have a beneficial impact on the local rate of ozone production in the VOC-sensitive regime, the ozone levels will not decrease until NO_x emissions are substantially lower, i.e., regulations on VOCs are needed in addition to continued controls on NOx emissions in China. These results can also partially explain why ozone pollution intensified in the past few years while $PM_{2.5}$ pollution abated. New datasets such as the updated 'bottom-up' emissions inventory for East Asia and high-resolution satellite observations such as TROPOMI products are needed to improve the modeling of ozone pollution in China, which can provide scientific evidence for future national and international regulations on air quality.

Supplementary Materials: The following supporting information can be downloaded at https://www.mdpi.com/article/10.3390/air2020011/s1, Figure S1: ARIAs flights over the NCP. Eleven research flights were conducted from May to mid-June 2016; Figure S2: CMEE Air quality monitoring sites in 2016; Figure S3: A plume observed over Xingtai during the flight on 11 June 2016; Figure S4: Comparison of mean CO and NO_2 concentrations in May and June 2016 over eastern China; Figure S5: A case study comparing aircraft observations and the CMAQ_baseline run results on 11 June 2016; Figure S6: Ratios of column contents of the CMAQ_baseline simulations and satellite observations; Figure S7: Similar to Figure 8, but shows differences between satellite observations and CMAQ simulations in May and June 2016; Figure S8: Similar to Figure 11, but compares CMEE observations and other CMAQ runs; Figure S9: Similar to Figure 5, but shows results from other CMAQ sensitivity experiments in the campaign region; Table S1: UMD aircraft instrumentation.

References

1. Shan, Y.; Guan, D.; Zheng, H.; Ou, J.; Li, Y.; Meng, J.; Mi, Z.; Liu, Z.; Zhang, Q. China CO_2 emission accounts 1997–2015. *Sci. Data* **2018**, *5*, 170201. [CrossRef] [PubMed]

2. Guan, D.B.; Meng, J.; Reiner, D.M.; Zhang, N.; Shan, Y.L.; Mi, Z.F.; Shao, S.; Liu, Z.; Zhang, Q.; Davis, S.J. Structural decline in China's CO_2 emissions through transitions in industry and energy systems. *Nat. Geosci.* **2018**, *11*, 551–555. [CrossRef]

3. Zhang, X.P.; Cheng, X.M. Energy consumption, carbon emissions, and economic growth in China. *Ecol. Econ.* **2009**, *68*, 2706–2712. [CrossRef]

4. Chan, C.K.; Yao, X. Air pollution in mega cities in China. *Atmos. Environ.* **2008**, *42*, 1–42. [CrossRef]

5. Fang, M.; Chan, C.K.; Yao, X.H. Managing air quality in a rapidly developing nation: China. *Atmos. Environ.* **2009**, *43*, 79–86. [CrossRef]

6. Chen, Y.Y.; Ebenstein, A.; Greenstone, M.; Li, H.B. Evidence on the impact of sustained exposure to air pollution on life expectancy from China's Huai River policy. *Proc. Natl. Acad. Sci. USA* **2013**, *110*, 12936–12941. [CrossRef] [PubMed]

7. Kan, H.D.; Chen, R.J.; Tong, S.L. Ambient air pollution, climate change, and population health in China. *Environ. Int.* **2012**, *42*, 10–19. [CrossRef] [PubMed]

8. Lelieveld, J.; Evans, J.S.; Fnais, M.; Giannadaki, D.; Pozzer, A. The contribution of outdoor air pollution sources to premature mortality on a global scale. *Nature* **2015**, *525*, 367–371. [CrossRef] [PubMed]

9. Tie, X.X.; Wu, D.; Brasseur, G. Lung cancer mortality and exposure to atmospheric aerosol particles in Guangzhou, China. *Atmos. Environ.* **2009**, *43*, 2375–2377. [CrossRef]

10. He, K.B.; Yang, F.M.; Ma, Y.L.; Zhang, Q.; Yao, X.H.; Chan, C.K.; Cadle, S.; Chan, T.; Mulawa, P. The characteristics of $PM_{2.5}$ in Beijing, China. *Atmos. Environ.* **2001**, *35*, 4959–4970. [CrossRef]

11. Sun, Y.L.; Zhuang, G.S.; Tang, A.H.; Wang, Y.; An, Z.S. Chemical characteristics of $PM_{2.5}$ and PM10 in haze-fog episodes in Beijing. *Environ. Sci. Technol.* **2006**, *40*, 3148–3155. [CrossRef] [PubMed]

12. Wang, Y.; Zhuang, G.S.; Tang, A.H.; Yuan, H.; Sun, Y.L.; Chen, S.A.; Zheng, A.H. The ion chemistry and the source of $PM_{2.5}$ aerosol in Beijing. *Atmos. Environ.* **2005**, *39*, 3771–3784. [CrossRef]

13. Zhang, R.; Jing, J.; Tao, J.; Hsu, S.C.; Wang, G.; Cao, J.; Lee, C.S.L.; Zhu, L.; Chen, Z.; Zhao, Y.; et al. Chemical characterization and source apportionment of $PM_{2.5}$ in Beijing: Seasonal perspective. *Atmos. Chem. Phys.* **2013**, *13*, 7053–7074. [CrossRef]

14. Zhang, X.Y.; Wang, Y.Q.; Niu, T.; Zhang, X.C.; Gong, S.L.; Zhang, Y.M.; Sun, J.Y. Atmospheric aerosol compositions in China: Spatial/temporal variability, chemical signature, regional haze distribution and comparisons with global aerosols. *Atmos. Chem. Phys.* **2012**, *12*, 779–799. [CrossRef]

15. Yang, F.; Tan, J.; Zhao, Q.; Du, Z.; He, K.; Ma, Y.; Duan, F.; Chen, G. Characteristics of $PM_{2.5}$ speciation in representative megacities and across China. *Atmos. Chem. Phys.* **2011**, *11*, 5207–5219. [CrossRef]

16. Ye, B.M.; Ji, X.L.; Yang, H.Z.; Yao, X.H.; Chan, C.K.; Cadle, S.H.; Chan, T.; Mulawa, P.A. Concentration and chemical composition of $PM_{2.5}$ in Shanghai for a 1-year period. *Atmos. Environ.* **2003**, *37*, 499–510. [CrossRef]

17. Li, Z.; Guo, J.; Ding, A.; Liao, H.; Liu, J.; Sun, Y.; Wang, T.; Xue, H.; Zhang, H.; Zhu, B. Aerosol and boundary-layer interactions and impact on air quality. *Natl. Sci. Rev.* **2017**, *4*, 810–833. [CrossRef]

18. Guo, J.; Miao, Y.; Zhang, Y.; Liu, H.; Li, Z.; Zhang, W.; He, J.; Lou, M.; Yan, Y.; Bian, L.; et al. The climatology of planetary boundary layer height in China derived from radiosonde and reanalysis data. *Atmos. Chem. Phys.* **2016**, *16*, 13309–13319. [CrossRef]

19. Ni, R.J.; Lin, J.T.; Yan, Y.Y.; Lin, W.L. Foreign and domestic contributions to springtime ozone over China. *Atmos. Chem. Phys.* **2018**, *18*, 11447–11469. [CrossRef]

20. Verstraeten, W.W.; Neu, J.L.; Williams, J.E.; Bowman, K.W.; Worden, J.R.; Boersma, K.F. Rapid increases in tropospheric ozone production and export from China. *Nat. Geosci.* **2015**, *8*, 690–695. [CrossRef]

21. Xue, L.K.; Wang, T.; Gao, J.; Ding, A.J.; Zhou, X.H.; Blake, D.R.; Wang, X.F.; Saunders, S.M.; Fan, S.J.; Zuo, H.C.; et al. Ground-level ozone in four Chinese cities: Precursors, regional transport and heterogeneous processes. *Atmos. Chem. Phys.* **2014**, *14*, 13175–13188. [CrossRef]

22. Wang, T.; Xue, L.K.; Brimblecombe, P.; Lam, Y.F.; Li, L.; Zhang, L. Ozone pollution in China: A review of concentrations, meteorological influences, chemical precursors, and effects. *Sci. Total Environ.* **2017**, *575*, 1582–1596. [CrossRef] [PubMed]

23. Liu, Z.; Wang, Y.; Gu, D.; Zhao, C.; Huey, L.G.; Stickel, R.; Liao, J.; Shao, M.; Zhu, T.; Zeng, L.; et al. Summertime photochemistry during CAREBeijing-2007: RO$_x$ budgets and O$_3$ formation. *Atmos. Chem. Phys.* **2012**, *12*, 7737–7752. [CrossRef]

24. Ma, M.; Gao, Y.; Wang, Y.; Zhang, S.; Leung, L.R.; Liu, C.; Wang, S.; Zhao, B.; Chang, X.; Su, H.; et al. Substantial ozone enhancement over the North China Plain from increased biogenic emissions due to heat waves and land cover in summer 2017. *Atmos. Chem. Phys.* **2019**, *19*, 12195–12207. [CrossRef]

25. Lu, X.; Hong, J.; Zhang, L.; Cooper, O.R.; Schultz, M.G.; Xu, X.; Wang, T.; Gao, M.; Zhao, Y.; Zhang, Y. Severe Surface Ozone Pollution in China: A Global Perspective. *Environ. Sci. Technol. Lett.* **2018**, *5*, 487–494. [CrossRef]

26. Li, K.; Jacob, D.J.; Liao, H.; Qiu, Y.; Shen, L.; Zhai, S.; Bates, K.H.; Sulprizio, M.P.; Song, S.; Lu, X.; et al. Ozone pollution in the North China Plain spreading into the late-winter haze season. *Proc. Natl. Acad. Sci. USA* **2021**, *118*, e2015797118. [CrossRef] [PubMed]

27. Li, K.; Jacob, D.J.; Liao, H.; Shen, L.; Zhang, Q.; Bates, K.H. Anthropogenic drivers of 2013–2017 trends in summer surface ozone in China. *Proc. Natl. Acad. Sci. USA* **2019**, *116*, 422–427. [CrossRef]

28. Zhao, C.; Wang, Y.; Zeng, T. East China Plains: A "Basin" of Ozone Pollution. *Environ. Sci. Technol.* **2009**, *43*, 1911–1915. [CrossRef] [PubMed]

29. WHO. *Health Aspects of Air Pollution with Particulate Matter, Ozone and Nitrogen Dioxide*; World Health Organization: Geneva, Switzerland, 2003.

30. Anderson, H.R. Air pollution and mortality: A history. *Atmos. Environ.* **2009**, *43*, 142–152. [CrossRef]

31. Jerrett, M.; Burnett, R.T.; Pope, C.A.; Ito, K.; Thurston, G.; Krewski, D.; Shi, Y.L.; Calle, E.; Thun, M. Long-Term Ozone Exposure and Mortality. *N. Engl. J. Med.* **2009**, *360*, 1085–1095. [CrossRef]

32. Chameides, W.L.; Li, X.S.; Tang, X.Y.; Zhou, X.J.; Luo, C.; Kiang, C.S.; St John, J.; Saylor, R.D.; Liu, S.C.; Lam, K.S.; et al. Is ozone pollution affecting crop yields in China? *Geophys. Res. Lett.* **1999**, *26*, 867–870. [CrossRef]

33. Ashmore, M.R. Assessing the future global impacts of ozone on vegetation. *Plant Cell Environ.* **2005**, *28*, 949–964. [CrossRef]

34. Adams, R.M.; Glyer, J.D.; Johnson, S.L.; McCarl, B.A. A reassessment of the economic-effects of ozone on United-States agriculture. *JAPCA J. Air Waste Manag. Assoc.* **1989**, *39*, 960–968.

35. Ramanathan, V.; Dickinson, R.E. Role of stratospheric ozone in the zonal and seasonal radiative energy-balance of the Earth-troposphere system. *J. Atmos. Sci.* **1979**, *36*, 1084–1104.

36. Pachauri, R.K.; Meyer, L.A. (Eds.) *Climate Change 2014: Synthesis Report. Contribution of Working Groups I, II and III to the Fifth Assessment Report of the Intergovernmental Panel on Climate Change*; IPCC: Geneva, Switzerland, 2014; 151p.

37. Lacis, A.A.; Wuebbles, D.J.; Logan, J.A. Radiative forcing of climate by changes in the vertical-distribution of ozone. *J. Geophys. Res. Atmos.* **1990**, *95*, 9971–9981. [CrossRef]

38. Logan, J.A.; Prather, M.J.; Wofsy, S.C.; McElroy, M.B. Tropospheric chemistry—A global perspective. *J. Geophys. Res. Ocean. Atmos.* **1981**, *86*, 7210–7254. [CrossRef]

39. Finlayson-Pitts, B.J.; Pitts, J.N. *Chemistry of the Upper and Lower Atmosphere*, 1st ed.; Academic Press: London, UK, 1999.

40. Thompson, A.M. The oxidizing capacity of the Earth's Atmosphere—Probable past and future changes. *Science* **1992**, *256*, 1157–1165. [CrossRef] [PubMed]

41. Young, P.J.; Archibald, A.T.; Bowman, K.W.; Lamarque, J.F.; Naik, V.; Stevenson, D.S.; Tilmes, S.; Voulgarakis, A.; Wild, O.; Bergmann, D.; et al. Pre-industrial to end 21st century projections of tropospheric ozone from the Atmospheric Chemistry and Climate Model Intercomparison Project (ACCMIP). *Atmos. Chem. Phys.* **2013**, *13*, 2063–2090. [CrossRef]

42. Stevenson, D.S.; Dentener, F.J.; Schultz, M.G.; Ellingsen, K.; van Noije, T.P.C.; Wild, O.; Zeng, G.; Amann, M.; Atherton, C.S.; Bell, N.; et al. Multimodel ensemble simulations of present-day and near-future tropospheric ozone. *J. Geophys. Res. Atmos.* **2006**, *111*, D08301. [CrossRef]

43. Jacob, D.J.; Logan, J.A.; Murti, P.P. Effect of rising Asian emissions on surface ozone in the United States. *Geophys. Res. Lett.* **1999**, *26*, 2175–2178. [CrossRef]

44. Derwent, R.G.; Stevenson, D.S.; Collins, W.J.; Johnson, C.E. Intercontinental transport and the origins of the ozone observed at surface sites in Europe. *Atmos. Environ.* **2004**, *38*, 1891–1901. [CrossRef]

45. Lin, J.T.; Wuebbles, D.J.; Liang, X.Z. Effects of intercontinental transport on surface ozone over the United States: Present and future assessment with a global model. *Geophys. Res. Lett.* **2008**, *35*, L02805. [CrossRef]

46. Crutzen, P.J. Photochemical reactions initiated by and influencing ozone in unpolluted tropospheric air. *Tellus* **1974**, *26*, 47–57. [CrossRef]

47. Fishman, J.; Solomon, S.; Crutzen, P.J. Observational and theoretical evidence in support of a significant insitu photo-chemical source of tropospheric ozone. *Tellus* **1979**, *31*, 432–446. [CrossRef]

48. Seinfeld, J.H.; Pandis, S.N. *Atmospheric Chemistry and Physics: From Air Pollution to Climate Change*, 2nd ed.; John Wiley & Sons, Inc.: Hoboken, NJ, USA, 2006.

49. Haagensmit, A.J. Chemistry and physiology of Los-Angeles smog. *Ind. Eng. Chem.* **1952**, *44*, 1342–1346. [CrossRef]

50. Zhao, B.; Wang, S.X.; Liu, H.; Xu, J.Y.; Fu, K.; Klimont, Z.; Hao, J.M.; He, K.B.; Cofala, J.; Amann, M. NO_x emissions in China: Historical trends and future perspectives. *Atmos. Chem. Phys.* **2013**, *13*, 9869–9897. [CrossRef]

51. Streets, D.G.; Bond, T.C.; Carmichael, G.R.; Fernandes, S.D.; Fu, Q.; He, D.; Klimont, Z.; Nelson, S.M.; Tsai, N.Y.; Wang, M.Q.; et al. An inventory of gaseous and primary aerosol emissions in Asia in the year 2000. *J. Geophys. Res. Atmos.* **2003**, *108*, 8809. [CrossRef]

52. Ohara, T.; Akimoto, H.; Kurokawa, J.; Horii, N.; Yamaji, K.; Yan, X.; Hayasaka, T. An Asian emission inventory of anthropogenic emission sources for the period 1980–2020. *Atmos. Chem. Phys.* **2007**, *7*, 4419–4444. [CrossRef]

53. Zhao, Y.; Zhang, J.; Nielsen, C.P. The effects of recent control policies on trends in emissions of anthropogenic atmospheric pollutants and CO_2 in China. *Atmos. Chem. Phys.* **2013**, *13*, 487–508. [CrossRef]

54. Lin, J.; Nielsen, C.P.; Zhao, Y.; Lei, Y.; Liu, Y.; McElroy, M.B. Recent Changes in Particulate Air Pollution over China Observed from Space and the Ground: Effectiveness of Emission Control. *Environ. Sci. Technol.* **2010**, *44*, 7771–7776. [CrossRef]

55. Gu, D.S.; Wang, Y.H.; Smeltzer, C.; Liu, Z. Reduction in NO_x Emission Trends over China: Regional and Seasonal Variations. *Environ. Sci. Technol.* **2013**, *47*, 12912–12919. [CrossRef]

56. Liu, F.; Zhang, Q.; Ronald, J.V.; Zheng, B.; Tong, D.; Yan, L.; Zheng, Y.X.; He, K.B. Recent reduction in NO_x emissions over China: Synthesis of satellite observations and emission inventories. *Environ. Res. Lett.* **2016**, *11*, 114002. [CrossRef]

57. Duncan, B.N.; Lamsal, L.N.; Thompson, A.M.; Yoshida, Y.; Lu, Z.F.; Streets, D.G.; Hurwitz, M.M.; Pickering, K.E. A space-based, high-resolution view of notable changes in urban NO_x pollution around the world (2005–2014). *J. Geophys. Res. Atmos.* **2016**, *121*, 976–996. [CrossRef]

58. Bo, Y.; Cai, H.; Xie, S.D. Spatial and temporal variation of historical anthropogenic NMVOCs emission inventories in China. *Atmos. Chem. Phys.* **2008**, *8*, 7297–7316. [CrossRef]

59. Kurokawa, J.; Ohara, T.; Morikawa, T.; Hanayama, S.; Janssens-Maenhout, G.; Fukui, T.; Kawashima, K.; Akimoto, H. Emissions of air pollutants and greenhouse gases over Asian regions during 2000–2008: Regional Emission inventory in ASia (REAS) version 2. *Atmos. Chem. Phys.* **2013**, *13*, 11019–11058. [CrossRef]

60. Wei, W.; Wang, S.X.; Hao, J.M.; Cheng, S.Y. Projection of anthropogenic volatile organic compounds (VOCs) emissions in China for the period 2010–2020. *Atmos. Environ.* **2011**, *45*, 6863–6871. [CrossRef]

61. Zhao, Y.; Mao, P.; Zhou, Y.; Yang, Y.; Zhang, J.; Wang, S.; Dong, Y.; Xie, F.; Yu, Y.; Li, W. Improved provincial emission inventory and speciation profiles of anthropogenic non-methane volatile organic compounds: A case study for Jiangsu, China. *Atmos. Chem. Phys.* **2017**, *17*, 7733–7756. [CrossRef]

62. Zhang, J.N.; Xiao, J.F.; Chen, X.F.; Liang, X.M.; Fan, L.Y.; Ye, D.Q. Allowance and allocation of industrial volatile organic compounds emission in China for year 2020 and 2030. *J. Environ. Sci.* **2018**, *69*, 155–165. [CrossRef]

63. Dodge, M. *Chemistry of Oxidant Formation: Implications for Designing Effective Control Strategies*; EPA/600/D-87/114 (NTIS PB87179990); U.S. Environmental Protection Agency: Washington, DC, USA, 1987.

64. Kleinman, L.I. Low and high NO_x tropospheric photochemistry. *J. Geophys. Res. Atmos.* **1994**, *99*, 16831–16838. [CrossRef]

65. Duncan, B.N.; Yoshida, Y.; Olson, J.R.; Sillman, S.; Martin, R.V.; Lamsal, L.; Hu, Y.T.; Pickering, K.E.; Retscher, C.; Allen, D.J.; et al. Application of OMI observations to a space-based indicator of NO_x and VOC controls on surface ozone formation. *Atmos. Environ.* **2010**, *44*, 2213–2223. [CrossRef]

66. Ring, A.M.; Canty, T.P.; Anderson, D.C.; Vinciguerra, T.P.; He, H.; Goldberg, D.L.; Ehrman, S.H.; Dickerson, R.R.; Salawitch, R.J. Evaluating commercial marine emissions and their role in air quality policy using observations and the CMAQ model. *Atmos. Environ.* **2018**, *173*, 96–107. [CrossRef]

67. Jin, X.; Fiore, A.M.; Murray, L.T.; Valin, L.C.; Lamsal, L.N.; Duncan, B.; Folkert Boersma, K.; De Smedt, I.; Abad, G.G.; Chance, K.; et al. Evaluating a Space-Based Indicator of Surface Ozone-NO_x-VOC Sensitivity Over Midlatitude Source Regions and Application to Decadal Trends. *J. Geophys. Res. Atmos.* **2017**, *122*, 10439–10461. [CrossRef]

68. Jin, X.; Holloway, T. Spatial and temporal variability of ozone sensitivity over China observed from the Ozone Monitoring Instrument. *J. Geophys. Res. Atmos.* **2015**, *120*, 7229–7246. [CrossRef]

69. Chou, C.C.K.; Tsai, C.-Y.; Shiu, C.-J.; Liu, S.C.; Zhu, T. Measurement of NO_y during Campaign of Air Quality Research in Beijing 2006 (CAREBeijing-2006): Implications for the ozone production efficiency of NO_x. *J. Geophys. Res. Atmos.* **2009**, *114*, D00G01. [CrossRef]

70. Xing, J.; Wang, S.X.; Jang, C.; Zhu, Y.; Hao, J.M. Nonlinear response of ozone to precursor emission changes in China: A modeling study using response surface methodology. *Atmos. Chem. Phys.* **2011**, *11*, 5027–5044. [CrossRef]

71. Wang, S.X.; Hao, J.M. Air quality management in China: Issues, challenges, and options. *J. Environ. Sci.* **2012**, *24*, 2–13. [CrossRef]

72. Wang, S.X.; Xing, J.; Zhao, B.; Jang, C.; Hao, J.M. Effectiveness of national air pollution control policies on the air quality in metropolitan areas of China. *J. Environ. Sci.* **2014**, *26*, 13–22. [CrossRef]

73. Yang, Q.; Wang, Y.; Zhao, C.; Liu, Z.; Gustafson, W.I., Jr.; Shao, M. NO_x Emission Reduction and its Effects on Ozone during the 2008 Olympic Games. *Environ. Sci. Technol.* **2011**, *45*, 6404–6410. [CrossRef] [PubMed]

74. Wang, W.; Li, X.; Cheng, Y.; Parrish, D.D.; Ni, R.; Tan, Z.; Liu, Y.; Lu, S.; Wu, Y.; Chen, S.; et al. Ozone pollution mitigation strategy informed by long-term trends of atmospheric oxidation capacity. *Nat. Geosci.* **2024**, *17*, 20–25. [CrossRef]

75. Qu, H.; Wang, Y.; Zhang, R.; Li, J. Extending Ozone-Precursor Relationships in China from Peak Concentration to Peak Time. *J. Geophys. Res. Atmos.* **2020**, *125*, e2020JD033670. [CrossRef]

76. Zhang, W.; Zhu, T.; Yang, W.; Bai, Z.; Sun, Y.L.; Xu, Y.; Yin, B.; Zhao, X. Airborne measurements of gas and particle pollutants during CAREBeijing-2008. *Atmos. Chem. Phys.* **2014**, *14*, 301–316. [CrossRef]

77. Wang, R.; Xu, X.B.; Jia, S.H.; Ma, R.S.; Ran, L.; Deng, Z.Z.; Lin, W.L.; Wang, Y.; Ma, Z.Q. Lower tropospheric distributions of O-3 and aerosol over Raoyang, a rural site in the North China Plain. *Atmos. Chem. Phys.* **2017**, *17*, 3891–3903. [CrossRef]

78. Huang, J.; Liu, H.; Crawford, J.H.; Chan, C.; Considine, D.B.; Zhang, Y.; Zheng, X.; Zhao, C.; Thouret, V.; Oltmans, S.J.; et al. Origin of springtime ozone enhancements in the lower troposphere over Beijing: In situ measurements and model analysis. *Atmos. Chem. Phys.* **2015**, *15*, 5161–5179. [CrossRef]

79. Dickerson, R.R.; Li, C.; Li, Z.; Marufu, L.T.; Stehr, J.W.; McClure, B.; Krotkov, N.; Chen, H.; Wang, P.; Xia, X.; et al. Aircraft observations of dust and pollutants over northeast China: Insight into the meteorological mechanisms of transport. *J. Geophys. Res. Atmos.* **2007**, *112*, D24S90. [CrossRef]

80. Ding, K.; Liu, J.; Ding, A.; Liu, Q.; Zhao, T.L.; Shi, J.; Han, Y.; Wang, H.; Jiang, F. Uplifting of carbon monoxide from biomass burning and anthropogenic sources to the free troposphere in East Asia. *Atmos. Chem. Phys.* **2015**, *15*, 2843–2866. [CrossRef]

81. Wang, F.; Li, Z.; Ren, X.; Jiang, Q.; He, H.; Dickerson, R.R.; Dong, X.; Lv, F. Vertical distributions of aerosol optical properties during the spring 2016 ARIAs airborne campaign in the North China Plain. *Atmos. Chem. Phys.* **2018**, *18*, 8995–9010. [CrossRef]

82. Wang, Y.; Li, Z.; Zhang, Y.; Du, W.; Zhang, F.; Tan, H.; Xu, H.; Fan, T.; Jin, X.; Fan, X.; et al. Characterization of aerosol hygroscopicity, mixing state, and CCN activity at a suburban site in the central North China Plain. *Atmos. Chem. Phys.* **2018**, *18*, 11739–11752. [CrossRef]

83. Li, Z.; Wang, Y.; Guo, J.; Zhao, C.; Cribb, M.C.; Dong, X.; Fan, J.; Gong, D.; Huang, J.; Jiang, M.; et al. East Asian Study of Tropospheric Aerosols and their Impact on Regional Clouds, Precipitation, and Climate (EAST-AIRCPC). *J. Geophys. Res. Atmos.* **2019**, *124*, 13026–13054. [CrossRef]

84. Zhang, R.; Wang, Y.; Li, Z.; Wang, Z.; Dickerson, R.R.; Ren, X.; He, H.; Wang, F.; Gao, Y.; Chen, X.; et al. Vertical profiles of cloud condensation nuclei number concentration and its empirical estimate from aerosol optical properties over the North China Plain. *Atmos. Chem. Phys.* **2022**, *22*, 14879–14891. [CrossRef]

85. Wang, Y.S.; Yao, L.; Wang, L.L.; Liu, Z.R.; Ji, D.S.; Tang, G.Q.; Zhang, J.K.; Sun, Y.; Hu, B.; Xin, J.Y. Mechanism for the formation of the January 2013 heavy haze pollution episode over central and eastern China. *Sci. China Earth Sci.* **2014**, *57*, 14–25. [CrossRef]

86. Zhao, P.S.; Dong, F.; He, D.; Zhao, X.J.; Zhang, X.L.; Zhang, W.Z.; Yao, Q.; Liu, H.Y. Characteristics of concentrations and chemical compositions for $PM_{2.5}$ in the region of Beijing, Tianjin, and Hebei, China. *Atmos. Chem. Phys.* **2013**, *13*, 4631–4644. [CrossRef]

87. Halliday, H.S.; DiGangi, J.P.; Choi, Y.; Diskin, G.S.; Pusede, S.E.; Rana, M.; Nowak, J.B.; Knote, C.; Ren, X.; He, H.; et al. Using Short-Term CO/CO_2 Ratios to Assess Air Mass Differences over the Korean Peninsula during KORUS-AQ. *J. Geophys. Res. Atmos.* **2019**, *124*, 10951–10972. [CrossRef]

88. Benish, S.E.; He, H.; Ren, X.; Roberts, S.J.; Salawitch, R.J.; Li, Z.; Wang, F.; Wang, Y.; Zhang, F.; Shao, M.; et al. Measurement report: Aircraft observations of ozone, nitrogen oxides, and volatile organic compounds over Hebei Province, China. *Atmos. Chem. Phys.* **2020**, *20*, 14523–14545. [CrossRef]

89. Wang, F.; Li, Z.; Jiang, Q.; Ren, X.; He, H.; Tang, Y.; Dong, X.; Sun, Y.; Dickerson, R.R. Comparative Analysis of Aerosol Vertical Characteristics over the North China Plain Based on Multi-Source Observation Data. *Remote Sens.* **2024**, *16*, 609. [CrossRef]

90. Taubman, B.F.; Hains, J.C.; Thompson, A.M.; Marufu, L.T.; Doddridge, B.G.; Stehr, J.W.; Piety, C.A.; Dickerson, R.R. Aircraft vertical profiles of trace gas and aerosol pollution over the mid-Atlantic United States: Statistics and meteorological cluster analysis. *J. Geophys. Res. Atmos.* **2006**, *111*, D10S07. [CrossRef]

91. Castellanos, P.; Luke, W.T.; Kelley, P.; Stehr, J.W.; Ehrman, S.H.; Dickerson, R.R. Modification of a commercial cavity ring-down spectroscopy NO_2 detector for enhanced sensitivity. *Rev. Sci. Instrum.* **2009**, *80*, 113107. [CrossRef] [PubMed]

92. Brent, L.C.; Thorn, W.J.; Gupta, M.; Leen, B.; Stehr, J.W.; He, H.; Arkinson, H.L.; Weinheimer, A.; Garland, C.; Pusede, S.E.; et al. Evaluation of the use of a commercially available cavity ringdown absorption spectrometer for measuring NO_2 in flight, and observations over the Mid-Atlantic States, during DISCOVER-AQ. *J. Atmos. Chem.* **2015**, *72*, 503–521. [CrossRef]

93. Luke, W.T.; Dickerson, R.R.; Ryan, W.F.; Pickering, K.E.; Nunnermacker, L.J. Tropospheric chemistry over the lower Great-Plains of the United States 2. Trace gas profiles and distributions. *J. Geophys. Res. Atmos.* **1992**, *97*, 20647–20670. [CrossRef]

94. Stehr, J.W.; Dickerson, R.R.; Hallock-Waters, K.A.; Doddridge, B.G.; Kirk, D. Observations of NO_y, CO, and SO_2 and the origin of reactive nitrogen in the eastern United States. *J. Geophys. Res. Atmos.* **2000**, *105*, 3553–3563. [CrossRef]

95. Ren, X.; Salmon, O.E.; Hansford, J.R.; Ahn, D.; Hall, D.; Benish, S.E.; Stratton, P.R.; He, H.; Sahu, S.; Grimes, C.; et al. Methane Emissions from the Baltimore-Washington Area Based on Airborne Observations: Comparison to Emissions Inventories. *J. Geophys. Res. Atmos.* **2018**, *123*, 8869–8882. [CrossRef]

96. Hains, J.C.; Taubman, B.F.; Thompson, A.M.; Stehr, J.W.; Marufu, L.T.; Doddridge, B.G.; Dickerson, R.R. Origins of chemical pollution derived from Mid-Atlantic aircraft profiles using a clustering technique. *Atmos. Environ.* **2008**, *42*, 1727–1741. [CrossRef]

97. He, H.; Loughner, C.P.; Stehr, J.W.; Arkinson, H.L.; Brent, L.C.; Follette-Cook, M.B.; Tzortziou, M.A.; Pickering, K.E.; Thompson, A.M.; Martins, D.K.; et al. An elevated reservoir of air pollutants over the Mid-Atlantic States during the 2011 DISCOVER-AQ campaign: Airborne measurements and numerical simulations. *Atmos. Environ.* **2014**, *85*, 18–30. [CrossRef]

98. Salmon, O.E.; Shepson, P.B.; Ren, X.; He, H.; Hall, D.L.; Dickerson, R.R.; Stirm, B.H.; Brown, S.S.; Fibiger, D.L.; McDuffie, E.E.; et al. Top-Down Estimates of NO$_x$ and CO Emissions from Washington, D.C.-Baltimore during the WINTER Campaign. *J. Geophys. Res. Atmos.* **2018**, *123*, 7705–7724. [CrossRef]

99. He, H.; Li, C.; Loughner, C.P.; Li, Z.; Krotkov, N.A.; Yang, K.; Wang, L.; Zheng, Y.; Bao, X.; Zhao, G.; et al. SO$_2$ over central China: Measurements, numerical simulations and the tropospheric sulfur budget. *J. Geophys. Res. Atmos.* **2012**, *117*, D00K37. [CrossRef]

100. Benish, S.E.; Salawitch, R.J.; Ren, X.; He, H.; Dickerson, R.R. Airborne Observations of CFCs Over Hebei Province, China in Spring 2016. *J. Geophys. Res. Atmos.* **2021**, *126*, e2021JD035152. [CrossRef]

101. Deeter, M.N.; Emmons, L.K.; Francis, G.L.; Edwards, D.P.; Gille, J.C.; Warner, J.X.; Khattatov, B.; Ziskin, D.; Lamarque, J.F.; Ho, S.P.; et al. Operational carbon monoxide retrieval algorithm and selected results for the MOPITT instrument. *J. Geophys. Res. Atmos.* **2003**, *108*, 4399. [CrossRef]

102. MOPITT Science Team. *MOPITT/Terra Level 3 Gridded Daily CO (on a Latitude/Longitude/Pressure Grid) Derived from Near and Thermal Infrared Radiances, Version 7*; NASA Atmospheric Science Data Center (ASDC): Hampton, VA, USA, 2013. [CrossRef]

103. Worden, H.M.; Deeter, M.N.; Edwards, D.P.; Gille, J.C.; Drummond, J.R.; Nedelec, P. Observations of near-surface carbon monoxide from space using MOPITT multispectral retrievals. *J. Geophys. Res. Atmos.* **2010**, *115*, D18314. [CrossRef]

104. Deeter, M.N.; Worden, H.M.; Edwards, D.P.; Gille, J.C.; Andrews, A.E. Evaluation of MOPITT retrievals of lower-tropospheric carbon monoxide over the United States. *J. Geophys. Res. Atmos.* **2012**, *117*, D13306. [CrossRef]

105. Levelt, P.F.; Hilsenrath, E.; Leppelmeier, G.W.; van den Oord, G.H.J.; Bhartia, P.K.; Tamminen, J.; de Haan, J.F.; Veefkind, J.P. Science objectives of the Ozone Monitoring Instrument. *IEEE Trans. Geosci. Remote Sens.* **2006**, *44*, 1199–1208. [CrossRef]

106. Krotkov, N.A.; Lamsal, L.N.; Marchenko, S.V.; Celarier, E.A.; Bucsela, E.J.; Swartz, W.H.; Veefkind, J.P. *OMI/Aura Nitrogen Dioxide (NO$_2$) Total and Tropospheric Column 1-Orbit L2 Swath 13×24 km V003*; Goddard Earth Sciences Data and Information Services Center (GES DISC): Greenbelt, MD, USA, 2018. [CrossRef]

107. Krotkov, N.A.; Lamsal, L.N.; Celarier, E.A.; Swartz, W.H.; Marchenko, S.V.; Bucsela, E.J.; Chan, K.L.; Wenig, M.; Zara, M. The version 3 OMI NO$_2$ standard product. *Atmos. Meas. Tech.* **2017**, *10*, 3133–3149. [CrossRef]

108. González Abad, G.; Liu, X.; Chance, K.; Wang, H.; Kurosu, T.P.; Suleiman, R. Updated Smithsonian Astrophysical Observatory Ozone Monitoring Instrument (SAO OMI) formaldehyde retrieval. *Atmos. Meas. Tech.* **2015**, *8*, 19–32. [CrossRef]

109. Chance, K. *OMI/Aura Formaldehyde (HCHO) Total Column 1-Orbit L2 Swath 13×24 km V003*; Goddard Earth Sciences Data and Information Services Center (GES DISC): Greenbelt, MD, USA, 2007. [CrossRef]

110. Boeke, N.L.; Marshall, J.D.; Alvarez, S.; Chance, K.V.; Fried, A.; Kurosu, T.P.; Rappenglück, B.; Richter, D.; Walega, J.; Weibring, P.; et al. Formaldehyde columns from the Ozone Monitoring Instrument: Urban versus background levels and evaluation using aircraft data and a global model. *J. Geophys. Res. Atmos.* **2011**, *116*, D05303. [CrossRef] [PubMed]

111. Millet, D.B.; Jacob, D.J.; Turquety, S.; Hudman, R.C.; Wu, S.; Fried, A.; Walega, J.; Heikes, B.G.; Blake, D.R.; Singh, H.B.; et al. Formaldehyde distribution over North America: Implications for satellite retrievals of formaldehyde columns and isoprene emission. *J. Geophys. Res. Atmos.* **2006**, *111*, D24S02. [CrossRef]

112. EPA. CMAQ (Version 5.3.3) Scientific Document. 2021. Available online: https://zenodo.org/records/5213949 (accessed on 1 June 2021).

113. Skamarock, W.C.; Klemp, J.B.; Dudhia, J.; Gill, D.O.; Barker, D.M.; Duda, M.G.; Huang, X.-Y.; Wang, W.; Powers, J.G. *A Description of the Advanced Research WRF Version 3*; NCAR Technical Note, NCAR/TN-475+STR; National Center for Atmospheric Research: Boulder, CO, USA, 2008; 113p.

114. Dee, D.P.; Uppala, S.M.; Simmons, A.J.; Berrisford, P.; Poli, P.; Kobayashi, S.; Andrae, U.; Balmaseda, M.A.; Balsamo, G.; Bauer, P.; et al. The ERA-Interim reanalysis: Configuration and performance of the data assimilation system. *Q. J. R. Meteorol. Soc.* **2011**, *137*, 553–597. [CrossRef]

115. Clough, S.A.; Shephard, M.W.; Mlawer, E.J.; Delamere, J.S.; Iacono, M.J.; Cady-Pereira, K.; Boukabara, S.; Brown, P.D. Atmospheric radiative transfer modeling: A summary of the AER codes. *J. Quant. Spectrosc. Radiat. Transf.* **2005**, *91*, 233–244. [CrossRef]

116. Pleim, J.E.; Xiu, A. Development and Testing of a Surface Flux and Planetary Boundary Layer Model for Application in Mesoscale Models. *J. Appl. Meteorol.* **1995**, *34*, 16–32. [CrossRef]

117. Xiu, A.; Pleim, J.E. Development of a Land Surface Model. Part I: Application in a Mesoscale Meteorological Model. *J. Appl. Meteorol.* **2001**, *40*, 192–209. [CrossRef]

118. Pleim, J.E. A Combined Local and Nonlocal Closure Model for the Atmospheric Boundary Layer. Part I: Model Description and Testing. *J. Appl. Meteorol. Climatol.* **2007**, *46*, 1383–1395. [CrossRef]

119. Kain, J.S. The Kain-Fritsch convective parameterization: An update. *J. Appl. Meteorol.* **2004**, *43*, 170–181. [CrossRef]

120. Hong, S.-Y.; Lim, J.-O. The WRF single-moment 6-class microphysics scheme (WSM6). *J. Korean Meteorol. Soc.* **2006**, *42*, 129–151.

121. Mazzuca, G.M.; Ren, X.R.; Loughner, C.P.; Estes, M.; Crawford, J.H.; Pickering, K.E.; Weinheimer, A.J.; Dickerson, R.R. Ozone production and its sensitivity to NO$_x$ and VOCs: Results from the DISCOVER-AQ field experiment, Houston 2013. *Atmos. Chem. Phys.* **2016**, *16*, 14463–14474. [CrossRef]

122. European Commission. Joint Research Centre (JRC)/Netherlands Environmental Assessment Agency (PBL). Emission Database for Global Atmospheric Research (EDGAR). Release Version 4.2. 2011. Available online: http://edgar.jrc.ec.europa.eu (accessed on 7 March 2017).

123. UNC. *SMOKE v4.7 User's Manual*; The Institute for the Environment, The University of North Carolina at Chapel Hill: Chapel Hill, NC, USA, 2019.

124. Yarwood, G.S.; Rao, S.T.; Yocke, M.; Whitten, G.Z. *Updates to the Carbon Bond Chemical Mechanism: CB05*; ENVIRON International Corp: Arlington, VA, USA, 2005.

125. Appel, K.W.; Pouliot, G.A.; Simon, H.; Sarwar, G.; Pye, H.O.T.; Napelenok, S.L.; Akhtar, F.; Roselle, S.J. Evaluation of dust and trace metal estimates from the Community Multiscale Air Quality (CMAQ) model version 5.0. *Geosci. Model Dev.* **2013**, *6*, 883–899. [CrossRef]

126. Yarwood, G.S.; Whitten, G.Z.; Jung, J.; Heo, G.; Allen, D. Development, Evaluation and Testing of Version 6 of the Carbon Bond Chemical Mechanism (CB6). 2010. Available online: https://www.tceq.texas.gov/assets/public/implementation/air/am/contracts/reports/pm/5820784005FY1026-20100922-environ-cb6.pdf (accessed on 1 June 2021).

127. Appel, K.W.; Napelenok, S.L.; Hogrefe, C.; Foley, K.M.; Pouliot, G.; Murphy, B.N.; Luecken, D.J.; Heath, N. Evaluation of the Community Multiscale Air Quality (CMAQ) Model Version 5.2. In Proceedings of the 2016 CMAS Conference, Chapel Hill, NC, USA, 24–26 October 2016.

128. Goldberg, D.L.; Vinciguerra, T.P.; Anderson, D.C.; Hembeck, L.; Canty, T.P.; Ehrman, S.H.; Martins, D.K.; Stauffer, R.M.; Thompson, A.M.; Salawitch, R.J.; et al. CAMx Ozone Source Attribution in the Eastern United States using Guidance from Observations during DISCOVER-AQ Maryland. *Geophys. Res. Lett.* **2016**, *43*, 2249–2258. [CrossRef] [PubMed]

129. Li, M.; Zhang, Q.; Kurokawa, J.; Woo, J.H.; He, K.B.; Lu, Z.F.; Ohara, T.; Song, Y.; Streets, D.G.; Carmichael, G.R.; et al. MIX: A mosaic Asian anthropogenic emission inventory under the international collaboration framework of the MICS-Asia and HTAP. *Atmos. Chem. Phys.* **2017**, *17*, 935–963. [CrossRef]

130. Heimburger, A.M.F.; Harvey, R.M.; Shepson, P.B.; Stirm, B.H.; Gore, C.; Turnbull, J.; Cambaliza, M.O.L.; Salmon, O.E.; Kerlo, A.E.M.; Lavoie, T.N.; et al. Assessing the optimized precision of the aircraft mass balance method for measurement of urban greenhouse gas emission rates through averaging. *Elem. Sci. Anthr.* **2017**, *5*, 26. [CrossRef]

131. Cambaliza, M.O.L.; Shepson, P.B.; Caulton, D.R.; Stirm, B.; Samarov, D.; Gurney, K.R.; Turnbull, J.; Davis, K.J.; Possolo, A.; Karion, A.; et al. Assessment of uncertainties of an aircraft-based mass balance approach for quantifying urban greenhouse gas emissions. *Atmos. Chem. Phys.* **2014**, *14*, 9029–9050. [CrossRef]

132. Jiang, Z.; Worden, J.R.; Jones, D.B.A.; Lin, J.T.; Verstraeten, W.W.; Henze, D.K. Constraints on Asian ozone using Aura TES, OMI and Terra MOPITT. *Atmos. Chem. Phys.* **2015**, *15*, 99–112. [CrossRef]

133. Zheng, B.; Chevallier, F.; Ciais, P.; Yin, Y.; Deeter, M.N.; Worden, H.M.; Wang, Y.L.; Zhang, Q.; He, K.B. Rapid decline in carbon monoxide emissions and export from East Asia between years 2005 and 2016. *Environ. Res. Lett.* **2018**, *13*, 044007. [CrossRef]

134. de Foy, B.; Lu, Z.; Streets, D.G.; Lamsal, L.N.; Duncan, B.N. Estimates of power plant NO_x emissions and lifetimes from OMI NO_2 satellite retrievals. *Atmos. Environ.* **2015**, *116*, 1–11. [CrossRef]

135. Qu, Z.; Henze, D.K.; Capps, S.L.; Wang, Y.; Xu, X.G.; Wang, J.; Keller, M. Monthly top-down NO_x emissions for China (2005–2012): A hybrid inversion method and trend analysis. *J. Geophys. Res. Atmos.* **2017**, *122*, 4600–4625. [CrossRef]

136. Wang, S.W.; Zhang, Q.; Streets, D.G.; He, K.B.; Martin, R.V.; Lamsal, L.N.; Chen, D.; Lei, Y.; Lu, Z. Growth in NO_x emissions from power plants in China: Bottom-up estimates and satellite observations. *Atmos. Chem. Phys.* **2012**, *12*, 4429–4447. [CrossRef]

137. Stavrakou, T.; Muller, J.F.; Bauwens, M.; De Smedt, I.; Lerot, C.; Van Roozendael, M.; Coheur, P.F.; Clerbaux, C.; Boersma, K.F.; van der A, R.; et al. Substantial Underestimation of Post-Harvest Burning Emissions in the North China Plain Revealed by Multi-Species Space Observations. *Sci. Rep.* **2016**, *6*, 32307. [CrossRef] [PubMed]

138. Canty, T.P.; Hembeck, L.; Vinciguerra, T.P.; Anderson, D.C.; Goldberg, D.L.; Carpenter, S.F.; Allen, D.J.; Loughner, C.P.; Salawitch, R.J.; Dickerson, R.R. Ozone and NO_x chemistry in the eastern US: Evaluation of CMAQ/CB05 with satellite (OMI) data. *Atmos. Chem. Phys.* **2015**, *15*, 10965–10982. [CrossRef]

139. Krotkov, N.A.; McLinden, C.A.; Li, C.; Lamsal, L.N.; Celarier, E.A.; Marchenko, S.V.; Swartz, W.H.; Bucsela, E.J.; Joiner, J.; Duncan, B.N.; et al. Aura OMI observations of regional SO_2 and NO_2 pollution changes from 2005 to 2015. *Atmos. Chem. Phys.* **2016**, *16*, 4605–4629. [CrossRef]

140. Li, M.; Zhang, Q.; Streets, D.G.; He, K.B.; Cheng, Y.F.; Emmons, L.K.; Huo, H.; Kang, S.C.; Lu, Z.; Shao, M.; et al. Mapping Asian anthropogenic emissions of non-methane volatile organic compounds to multiple chemical mechanisms. *Atmos. Chem. Phys.* **2014**, *14*, 5617–5638. [CrossRef]

141. Kleinman, L.I. Ozone process insights from field experiments—Part II: Observation-based analysis for ozone production. *Atmos. Environ.* **2000**, *34*, 2023–2033. [CrossRef]

142. Sillman, S. The relation between ozone, NO_x and hydrocarbons in urban and polluted rural environments. *Atmos. Environ.* **1999**, *33*, 1821–1845. [CrossRef]

143. Schroeder, J.R.; Crawford, J.H.; Fried, A.; Walega, J.; Weinheimer, A.; Wisthaler, A.; Muller, M.; Mikoviny, T.; Chen, G.; Shook, M.; et al. New insights into the column CH_2O/NO_2 ratio as an indicator of near-surface ozone sensitivity. *J. Geophys. Res. Atmos.* **2017**, *122*, 8885–8907. [CrossRef]

144. Xing, J.; Ding, D.; Wang, S.X.; Zhao, B.; Jang, C.; Wu, W.J.; Zhang, F.F.; Zhu, Y.; Hao, J.M. Quantification of the enhanced effectiveness of NO_x control from simultaneous reductions of VOC and NH_3 for reducing air pollution in the Beijing-Tianjin-Hebei region, China. *Atmos. Chem. Phys.* **2018**, *18*, 7799–7814. [CrossRef]

145. Goldberg, D.L.; Saide, P.E.; Lamsal, L.N.; de Foy, B.; Lu, Z.; Woo, J.H.; Kim, Y.; Kim, J.; Gao, M.; Carmichael, G.; et al. A top-down assessment using OMI NO_2 suggests an underestimate in the NO_x emissions inventory in Seoul, South Korea, during KORUS-AQ. *Atmos. Chem. Phys.* **2019**, *19*, 1801–1818. [CrossRef]

146. Miyazaki, K.; Sekiya, T.; Fu, D.; Bowman, K.W.; Kulawik, S.S.; Sudo, K.; Walker, T.; Kanaya, Y.; Takigawa, M.; Ogochi, K.; et al. Balance of Emission and Dynamical Controls on Ozone during the Korea-United States Air Quality Campaign from Multiconstituent Satellite Data Assimilation. *J. Geophys. Res. Atmos.* **2019**, *124*, 387–413. [CrossRef] [PubMed]

147. Lin, J.T.; McElroy, M.B.; Boersma, K.F. Constraint of anthropogenic NO$_x$ emissions in China from different sectors: A new methodology using multiple satellite retrievals. *Atmos. Chem. Phys.* **2010**, *10*, 63–78. [CrossRef]

148. Gaudel, A.; Cooper, R.; Ancellet, G.; Barret, B.; Boynard, A.; Burrows, J.; Clerbaux, C.; Coheur, P.-F.; Cuesta, J.; Cuevas, E. Tropospheric Ozone Assessment Report: Present-day distribution and trends of tropospheric ozone relevant to climate and global atmospheric chemistry model evaluation. *Elem. Sci. Anthr.* **2018**, *6*, 39. [CrossRef]

149. Junge, C.E. Global ozone budget and exchange between stratosphere and troposphere. *Tellus* **1962**, *14*, 363–377. [CrossRef]

150. Lin, M.; Fiore, A.M.; Cooper, O.R.; Horowitz, L.W.; Langford, A.O.; Levy Ii, H.; Johnson, B.J.; Naik, V.; Oltmans, S.J.; Senff, C.J. Springtime high surface ozone events over the western United States: Quantifying the role of stratospheric intrusions. *J. Geophys. Res. Atmos.* **2012**, *117*, D00V22. [CrossRef]

151. Liu, H.; Jacob, D.J.; Chan, L.Y.; Oltmans, S.J.; Bey, I.; Yantosca, R.M.; Harris, J.M.; Duncan, B.N.; Martin, R.V. Sources of tropospheric ozone along the Asian Pacific Rim: An analysis of ozonesonde observations. *J. Geophys. Res. Atmos.* **2002**, *107*, 4573. [CrossRef]

152. Wang, H.; Wang, W.; Shangguan, M.; Wang, T.; Hong, J.; Zhao, S.; Zhu, J. The Stratosphere-to-Troposphere Transport Related to Rossby Wave Breaking and Its Impact on Summertime Ground-Level Ozone in Eastern China. *Remote Sens.* **2023**, *15*, 2647. [CrossRef]

153. Chen, Z.; Liu, J.; Cheng, X.; Yang, M.; Shu, L. Stratospheric influences on surface ozone increase during the COVID-19 lockdown over northern China. *npj Clim. Atmos. Sci.* **2023**, *6*, 76. [CrossRef]

154. Xue, C.; Ye, C.; Lu, K.; Liu, P.; Zhang, C.; Su, H.; Bao, F.; Cheng, Y.; Wang, W.; Liu, Y.; et al. Reducing Soil-Emitted Nitrous Acid as a Feasible Strategy for Tackling Ozone Pollution. *Environ. Sci. Technol.* **2024**, *58*, 9227–9235. [CrossRef]